Macalester Journal of Physics and Astronomy

Volume 8
Issue 1 *Spring 2020*

Article 15

May 2020

Nitrogen Vacancy Center Optical Magnetometry of a Barium-Iron-Cobalt Superconductor

William Setterberg
Macalester College, wsetterb@macalester.edu

Nitrogen Vacancy Center Optical Magnetometry of a Barium-Iron-Cobalt Superconductor

Abstract

Experimentally probing the intrinsic properties of superconductors—such as the London penetration depth λ and the critical fields H_{c1} and H_{c2}—poses a difficult task. Various sample- and measurement-related factors can impact the efficacy of results obtained for λ or H_{c1}, such as perturbations to the magnetic properties of a superconducting sample or crystalline defects. One measurement technique that can minimize the impact of both of these issues is known as Nitrogen Vacancy (NV) center magnetometry. In this work, we use NV center magnetometry to perform minimally-invasive measurements of the lower critical field H_{c1} and the London penetration depth λ on a sample of $Ba(Fe_{1-x}Co_x)_2As_2$, x = 7.4% (BaCo122).

Keywords

superconductivity nv center nitrogen vacancy pnictide iron-based magnetometry

NITROGEN VACANCY CENTER OPTICAL MAGNETOMETRY OF A BARIUM-IRON-COBALT SUPERCONDUCTOR

WILLIAM SETTERBERG

Bachelor of Arts in Physics
Advisor: Dr. James N. Heyman

Department of Physics and Astronomy
Macalester College
St. Paul, Minnesota, USA

Date submitted: May 4, 2020

For my sister Katie, my brother Michael, and my brother Thomas. Maybe this will be an interesting read for you some day.

ABSTRACT

Experimentally probing the intrinsic properties of superconductors—such as the London penetration depth λ and the critical fields H_{c1} and H_{c2}—poses a difficult task. Various sample- and measurement-related factors can impact the efficacy of results obtained for λ or H_{c1}, such as perturbations to the magnetic properties of a superconducting sample or crystalline defects. One measurement technique that can minimize the impact of both of these issues is known as Nitrogen Vacancy (NV) center magnetometry. In this work, we use NV center magnetometry to perform minimally-invasive measurements of the lower critical field H_{c1} and the London penetration depth λ on a sample of $Ba(Fe_{1-x}Co_x)_2As_2$, $x = 7.4\%$ (BaCo122).

ACKNOWLEDGMENTS

There are several individuals I'd like to thank for supporting me during this work: scientists, faculty, and friends. I would like to first thank Naufer Nusran and the rest of the Iowa State University/Ames Lab team for affording me the opportunity to work on this superconductivity project. I want to earnestly thank Kamal Joshi, an Iowa State University graduate student, for guiding me for an entire summer of research and answering my many, *many* questions over the past several months—without his support, I would be lost. I want to further thank Professor James Heyman for serving as my adviser both on this project and during my career at Macalester. I wish to also thank Professor Jim Doyle for serving on my thesis committee and helping me work my way through physics as a whole. Finally, I wish to thank my loving friends and family that have supported me during this long word-journey.

It also seems fitting to include the important cookie-cutter acknowledgment of funding and support from Ames Lab in this section:

> *Work at the Ames Laboratory was supported by the U.S. Department of Energy Office of Science Science Undergraduate Laboratory Internship (SULI) program under its contract with Iowa State University, Contract No. DE-AC02-07CH11358. William is grateful to the DOE for the assistantship and opportunity to participate in the SULI program.*

CONTENTS

LIST OF FIGURES

LIST OF TABLES

Part I

INTRODUCTION

1

OVERVIEW

Superconductivity is a state of matter in which some materials under certain conditions exhibit identically zero electrical resistance and near-perfect magnetic field expulsion. As an experimental fact, superconductivity was discovered shortly after helium was first liquefied in the early twentieth century, and it took nearly fifty years to develop a theory that could describe it effectively. This is in part because superconductivity is inherently a quantum mechanical phenomenon—the superconducting state is essentially a Bose-Einstein condensate of electron pairs. This being said, we still do not understand all of its intricacies: we cannot predict what kinds of materials will exhibit superconductivity, for example. However, we *do* have robust models for the mechanisms of superconductivity in different kinds of materials. Not surprisingly, different superconducting materials exhibit different properties, and have different applications.

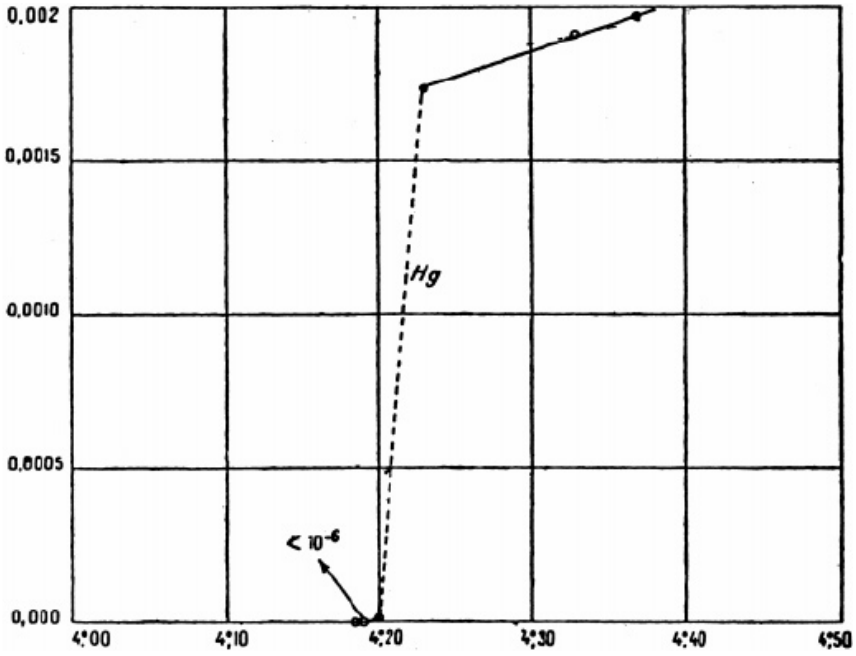

Figure 1.1: Heinrich Onnes' original 1911 plot of resistance versus temperature showing the superconducting transition of mercury (Hg) at around 4.2 Kelvin, the boiling point of Helium. At the time, Onnes thought that the resistance dropped to a very small value below the transition temperature; we now know that below this temperature, the resistance of a superconductor is *identically* zero [11].

Nowadays, superconductivity has several important applications. Magnetic resonance imaging (MRI), commonly used to image brains and other organs, relies on niobium-titanium (NbTi) superconducting wires to generate strong magnetic fields. MRI would be impossible without superconductors: if normal wires were used, they would melt almost immediately due to the large currents needed to generate the required magnetic field strength. Maglev train systems also use superconducting materials to generate strong magnetic fields for levitation; some of these trains can be found in regions of Japan, China, Germany, and other countries. Both Maglev systems and MRI machines require the superconductors to be cooled to very low temperatures for proper operation, which requires (expensive) liquid helium. So, high-temperature superconductors are an attractive goal, and this goal is one reason scientists are searching for new superconductors.

In addition to the development of these applications, our understanding of superconductivity has developed over the years. We have known since about the 1940s or 1950s that superconductivity is a thermodynamically stable state of matter—materials will spontaneously become superconducting under the right conditions. In fact, it is likely that part of the interior of Jupiter is comprised of a mass of superconducting hydrogen. A famous theory of superconductivity, BCS theory, predicts that hydrogen will become superconducting at around room temperature under pressures $P \sim 1000$ GPa. Thus, it is plausible that there are millions of tons of superconducting hydrogen inside of Jupiter, which may aid in making Jupiter's magnetosphere the largest structure in the Solar System, aside from structures associated with the Sun.

Aside from elemental superconductors like lead and hydrogen, there exist complex, compound superconductors. Some of these materials maintain superconductivity up to temperatures close to 300 K, room temperature. These are the so-called cuprate superconductors, whose crystalline structures contain copper oxide components. These materials were a particular surprise to the superconductivity community because they contain oxides and are essentially ceramics at room temperature. Another strange brand of superconductors are the so-called pnictide superconductors, many of which contain iron. These Fe-based superconductors are again unusual because of iron's magnetic properties. Iron is ferromagnetic, which is itself a quantum mechanical phenomenon like superconductivity. So, the presence of iron in superconductors provides a competing thermodynamically stable state (ferromagnetic or antiferromagnetic ordering) in these pnictide superconductors. In fact, near the superconducting temperature of certain pnictides, a phase transition from the superconducting state to the ferromagnetic or antiferromagnetic state can be observed [9].

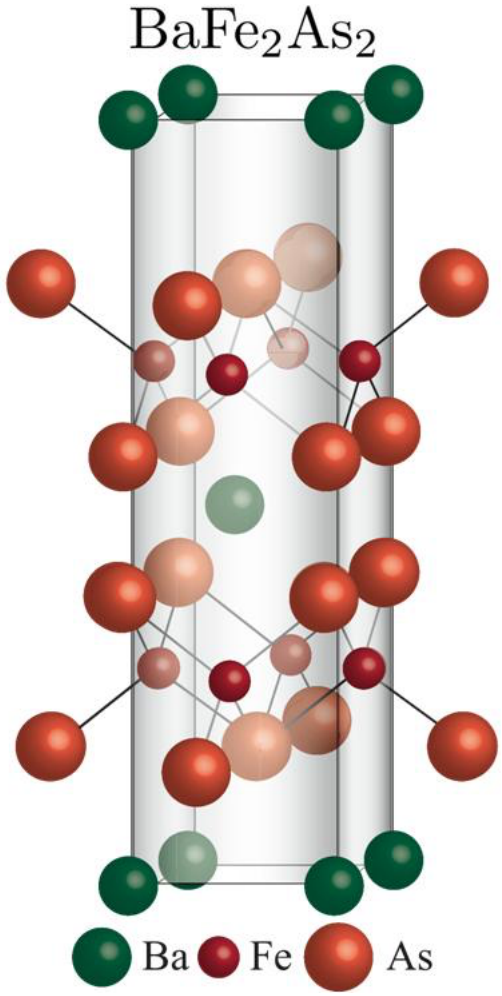

Figure 1.2: Structure of the BaCo122 superconductor, with no dopants. In our case, 7% of the iron is replaced with cobalt. Image from Fujimori Atsushi [4].

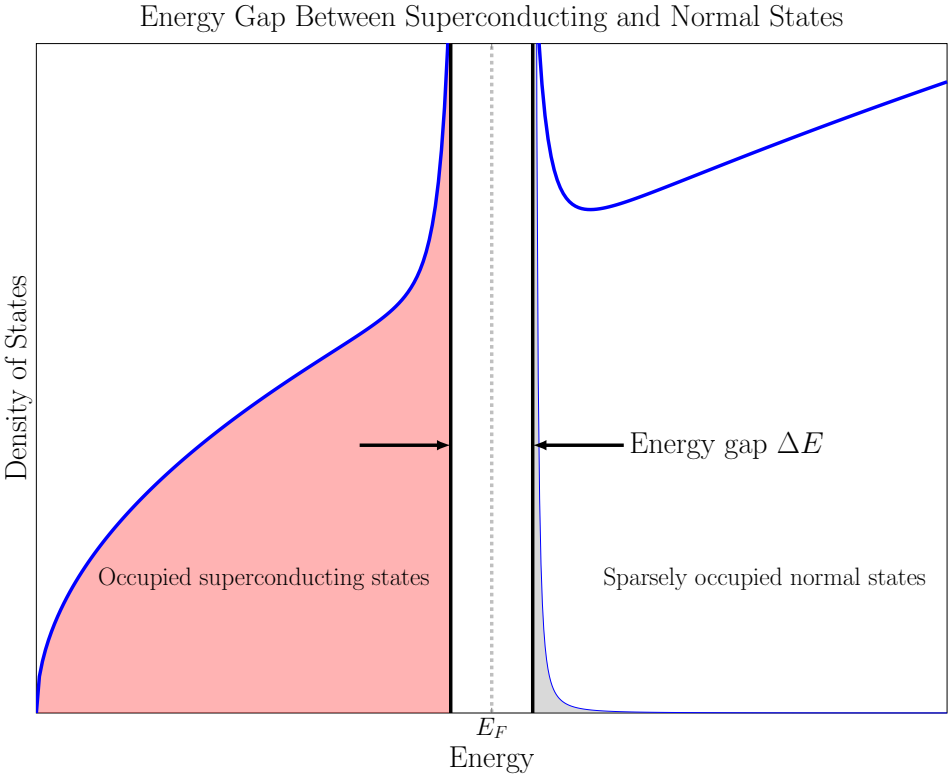

Figure 1.3: Simple depiction of energy gap ΔE between the superconducting (red, left) and normal (gray, right) density of states within a superconductor. Near absolute zero, nearly all electrons enter the superconducting state, and they can be described nicely by a *single* wavefunction.

This thesis focuses on the pnictide superconductor $Ba(Fe_{1-x}Co_x)_2As_2$, $x = 7.4\%$, which we refer to with the shorthand BaCo122, based on the compound name. BaCo122 is a member of the so-called 122 Iron Arsenides (hyperlink). The structure of BaCo122 can be seen in Figure 1.2. Substituting cobalt for 7.4% of the original iron in this compound maximizes the superconducting transition temperature with respect to the percentage of cobalt in the material [9]. This superconductor has a critical (superconducting transition) temperature of $T_c \approx 22.4$ K, and in addition to exhibiting phase transitions between the superconducting and antiferromagnetic states exhibits phase transitions that occur due to a change in crystalline structure. In short: it's a complex material.

One important area of interest relating to BaCo122 and other pnictide superconductors has to do with the quantum mechanical symmetries of the superconducting wavefunction. Because of the way electrons pair up in the superconducting state, there exists an energy gap between the superconducting and normal states, a simple depiction of which can be seen in Figure 1.3. In BCS theory—the first theory to successfully describe super-

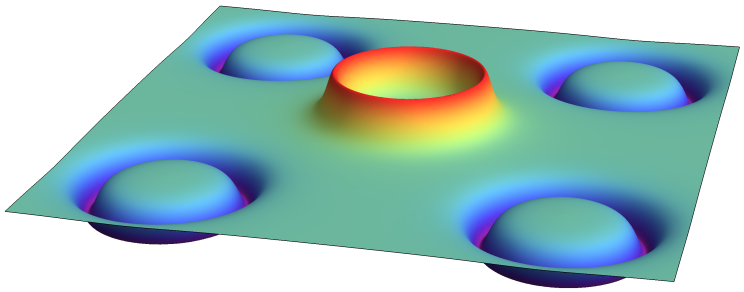

Figure 1.4: Cartoon of a what an $s_{\pm}$ material looks like in momentum space. The xy plane represents momentum components k_x and k_y and the vertical axis the magnitude of the energy gap between the normal and superconducting states. For electron-like superconducting charge carriers, the angular part of the wavefunction is positive; for hole-like carriers, it is negative. In BaCo122, there may be additional information important to its superconductivity mechanism that is encoded in variations of the *phase* of the wavefunction. This additional structure would cause the circular peaks in this figure to take on more structure.

conductivity microscopically—this energy gap is symmetric with respect to electron momentum. In more recently discovered superconductors, the superconducting energy gap *depends on electron momentum*. The way that these energy gaps depend on momentum has symmetry similar to the s and d orbitals of atoms. So, uniform energy gaps are called s-wave superconductors, and nonuniform energy gaps go by different names: p-wave, d-wave, f-wave, etc. For example, most elemental superconductors are s-wave, and the so-called Cuprate superconductors (hyperlink) are known to have d-wave symmetry.

The symmetry of the BaCo122 superconducting wavefunction is widely believed to exhibit $s_{\pm}$ symmetry, meaning that the sign on the angular part of the superconducting wavefunction is different for hole-like superconducting carriers and electron-like superconducting carriers [6]. A simplified depiction of this phenomenon can be seen in Figure 1.4. In the case of BaCo122 and other Fe-based pnictide superconductors, there may be even more information encoded in the phase of the wavefunction. That is, there could be more structure than just a sign change on the phase. The technique employed in this work (Nitrogen Vacancy center magnetometry) isn't capable of measuring this structure, but it may be possible to measure

this phase structure using a modified version of the technique used in this work. This idea will be discussed further at the end of this work.

Now, in order to understand the inner-workings of BaCo122, like its wavefunction symmetry, we should study its magnetic behavior: magnetic fields are expelled from superconductors, so it would make sense that by studying the magnetic fields *near* a superconductor, we can learn more about its properties. There are various techniques available to study the magnetic fields around superconductors, such as Superconducting Quantum Interference Devices (SQUIDs), Tunnel Diode Resonance (TDR), Magnetic Force Microscopy (MFM), Muon Spin Resonance (μSR), and the technique employed in this work, NV (nitrogen vacancy) center magnetometry. Each of these techniques has its own unique advantages and drawbacks. As can be seen in Figure 3.2, an NV center consists of a nitrogen atom and an adjacent vacancy in the diamond lattice. We can use this defect in diamond to measure the magnetic fields very close to the surface of the superconductor. Here are some advantages of NV centers when used as optical magnetometers:

- NV centers minimally perturb the system of interest ($\mu \sim \mu_B$, similar to that of an atom);
- They offer a noninvasive approach to measuring magnetic fields near superconductors (via an optical readout);
- They offer diffraction-limited spatial resolution;
- They are embedded in the robust structure of diamond, and have predictable properties at both room temperature and near absolute zero;
- They can measure the absolute value of the penetration depth.

In this work, we use many thousands of NV centers embedded about 20 nm deep into the surface of flat piece of electronics-grade diamond as the core of our magnetometer; this is known as *ensemble NV center magnetometry*. We use this NV center configuration in conjunction with a confocal microscope in order to collect fluorescence from the NV centers. This fluorescence carries with it information on the magnetic field near a given superconductor. A confocal microscope essentially places a small pinhole around the focus of a primary lens in order to reject light that originates from outside the focal volume of the microscope, which improves the signal to noise ratio of the system.

Once we collect information on the magnetic fields near a given superconductor, we can use this information to understand its fundamental properties, such as the length scale over which the superconducting

wavefunction can vary rapidly and the depth to which a magnetic field penetrates. Furthermore, before this work, NV center magnetometry had not been used to measure the temperature-dependence of the *London penetration depth* λ, which is the length scale over which an applied magnetic field penetrates the surface of a given superconductor. That is, **for the first time,** we use NV center magnetometry to measure the absolute value of the penetration depth in a superconductor, in our case $Ba(Fe_{1-x}Co_x)_2As_2$, $x = 7.4\%$. We show that NV center magnetometry is an accurate and minimally-invasive method for measuring the penetration depth λ as a function of temperature.

Let's recap: we have known about superconductors for over 100 years, and have several important applications. They exhibit zero electrical resistance and expel magnetic field when cooled below a certain critical temperature T_c, typically on the order of $1 - 100$ K. Their underlying physics is complicated and quantum-mechanical by nature. The energy gap between the superconducting and normal states can depend on momentum, and we can learn about the superconductor structure by probing the London penetration depth λ. In this instance, we use NV center magnetometry to measure the magnetic properties of BaCo122 as a function of temperature for the first time with this technique.

2

SUPERCONDUCTIVITY THEORY

Our understanding of superconductivity has evolved over time. We now understand that many materials including room-temperature insulators can become superconductors under the right conditions. Often, a material enters the superconducting state simply by being cooled below a *critical temperature*, or *superconducting transition temperature*, denoted T_c. Once a superconductor is cooled below its critical temperature T_c, it begins to exhibit two defining properties:

1. A superconductor cooled below a certain *critical temperature* T_c has identically zero electrical resistance.

2. A superconductor at a temperature $T < T_c$ will expel magnetic magnetic induction **B** from its interior, up to a certain applied critical field strength H_c. This magnetic flux expulsion is known as the *Meissner effect*.

Along with these defining properties, it will be useful moving forward to discuss in qualitative terms some length scales intrinsic to superconductors, known as the London penetration depth λ and the coherence length ξ. The London penetration depth λ has to do with the interaction of magnetic fields with superconductors. The coherence length ξ has to do with the properties of the superconducting wavefunction—yes, *the* superconducting wavefunction. Superconductivity is inherently a quantum mechanical phenomenon, so it's possible (necessary, in fact) to describe the superconducting charge carriers with a *single* wavefunction. **In simple, precise terms, the coherence length ξ is the length scale over which the superconducting wavefunction can vary rapidly: if it attempts to vary over a length scale shorter than ξ, superconductivity will be destroyed.** In the case of our BaCo122 sample, we have $\xi \sim 5$ nm.

The other length scale of interest is known as the London penetration depth λ. **The London penetration depth λ is the depth to which a magnetic field penetrates the surface of a superconductor, typically on the order of tens or hundreds of nanometers, as is the case with this BaCo122 sample.**

The relative magnitudes of the London penetration depth λ and the coherence length ξ define two different types of superconductors. In order to discuss how this happens, we must first define how *all* superconductors behave in magnetic fields. For both Type I and Type II superconductors,

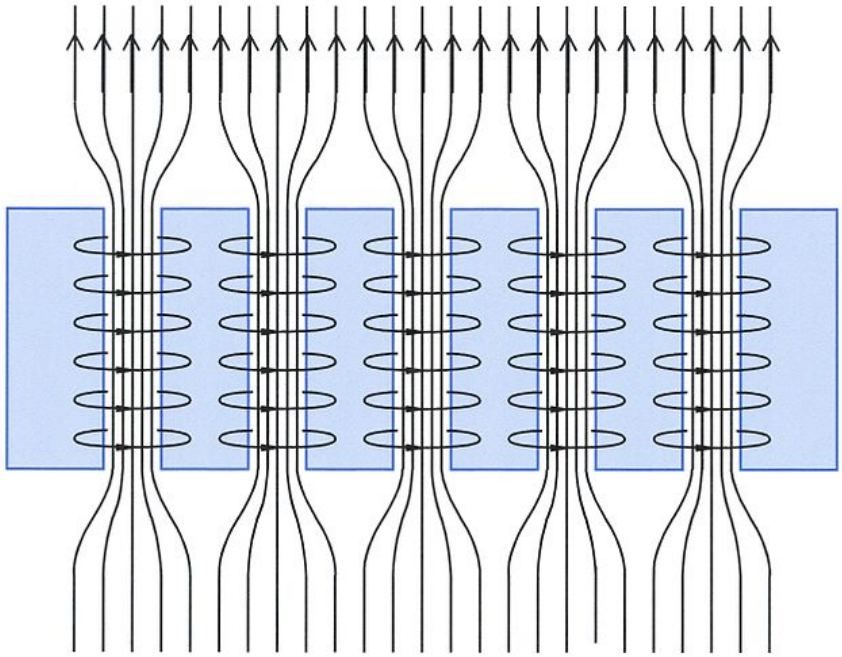

Figure 2.1: Quantized units of magnetic flux (Abrikosov vortices) penetrate Type II superconductors at applied field strengths H equal to or greater than the lower critical field H_{c1}. Superconducting shielding currents surround the normal regions. Image taken from Wikiepdia [3].

there exists some applied magnetic field strength H_c at which the superconducting state becomes energetically unfavorable and spontaneously breaks down. This is known as a *critical field*. For Type I superconductors, there exists only one critical field. For Type II superconductors, there are *two* critical fields—a lower critical field H_{c1} and an upper critical field H_{c2}. At the lower critical field, the superconductor enters a part-normal, part-superconducting state; at the upper critical field, superconductivity is destroyed. To put it simply: magnetic fields perturb the superconducting state, but the form of this perturbation depends on the type of superconductor.

In Type I superconductors, $\xi \gg \lambda$, i.e. the magnetic field drops off on a length scale shorter than the wavefunction can vary quickly, so there exists only *one* critical field. In Type II superconductors, $\xi \ll \lambda$, so the superconducting wavefunction can actually vary on length scales much *shorter* than the magnetic field penetration depth. This fast-varying nature of the wavefunction in Type II superconductors permits the formation of an intermediate state, part "normal" and part superconducting, known as a *vortex state*, named as such because of the way magnetic flux quanta penetrate the superconducting sample. A depiction of this state can be

seen in Figure 2.1. **In sum, Type I and Type II superconductors differ in magnetic properties because of differences in their intrinsic length scales λ and ξ.**

Because expulsion of magnetic field is intrinsic to superconductors, and because the superconducting state is thermodynamically stable, it's possible to relate the intrinsic length scales λ and ξ to thermodynamic properties of the superconducting state. In fact, before we derive expressions for ξ and λ, we will discuss the *energy gap* between the superconducting and normal states, and use this as a springboard into discussing λ and ξ.

For the remainder of this chapter, we will develop the mathematics behind the ideas discussed above. First, we will examine a connection between the thermodynamic stability of the superconducting state and applied magnetic fields. Next, we will develop the ideas of the coherence length and London penetration depth from a quantum mechanical perspective. Finally, we will interpret all of these mathematical pieces as a cohesive whole and transition into how we can use NV magnetometry to measure these intrinsic quantities.

2.1 MAGNETISM, THERMODYNAMICS, AND THE SUPERCONDUCTING STATE

In this section, we will develop what it means for superconductivity to be thermodynamically stable from the standpoint of the critical field H_c. As a reminder, the critical field H_c is the applied magnetic field strength at which the superconducting state is destroyed. To start, we need to differentiate between **H** and **B**. In SI units, the applied magnetic field is defined as follows:

$$\mathbf{H} \equiv \frac{1}{\mu_0}\mathbf{B} - \mathbf{M},$$

where **M** is the *magnetization* of the sample. This makes qualitative sense: the applied field is just the difference between the total field and the field induced in the sample. In magnetically linear materials, we can write the magnetization in the following form:

$$\mathbf{M} = \chi_v \mathbf{H}, \tag{2.1}$$

where χ_v is the *magnetic susceptibility* of the sample, which is well-defined for magnetically linear samples and intrinsic to the material. Thus, we can rewrite the applied field as follows:

$$\begin{aligned} \mathbf{H} &= \frac{1}{\mu_0}\mathbf{B} - \chi_v \mathbf{H}. \\ \Rightarrow \mathbf{B} &= \mu_0 \left(1 + \chi_v\right) \mathbf{H}. \end{aligned}$$

Inside of a superconductor, $\mathbf{B} = 0$. Thus, $\chi_v \equiv -1$ for an ideal superconductor, such that $\mathbf{B} = \mu_0(1-1)\mathbf{H} = 0$. At the critical field H_c, there is a transition in χ_v where the end result is that $\chi_v \to 0$, i.e. the material returns to normal. If we take $\chi_v = -1$ and use Equation 2.1, we find:

$$\begin{aligned} \mathbf{B} &= 0 \\ &= \mu_0(1-1)\mathbf{H} \\ &= \mu_0(1-\chi_v)\mathbf{H} \\ &= \mu_0\mathbf{H} - \mu_o\chi_v\mathbf{H} \\ \Rightarrow 0 &= \mu_0\mathbf{H} - \mu_0\mathbf{M} \\ \Rightarrow \left|\frac{\mathbf{M}}{\mathbf{H}}\right| &= -1 \text{ for } H < H_c. \end{aligned} \tag{2.2}$$

This fact will come in handy shortly.

As a next step in this thermodynamic analysis, let's consider the work done per unit volume on a superconductor brought from $r = \infty$ into a certain field strength B^*, holding temperature constant:

$$W_s = -\int_0^{B^*} \mathbf{M} \cdot d\mathbf{B}$$

where the subscript s indicates work on the superconducting sample. The units of the above expression make sense: $[\mathbf{M} \cdot \mathbf{B}] = [\mathrm{A/m}] \cdot [\mathrm{T}] = [\mathrm{A/m}] \cdot \left[\mathrm{kg/A/s^2}\right] = \left[\mathrm{J/m^3}\right]$, which is exactly an energy density, or work per unit volume. Continuing with this treatment, if we incorporate Equation 2.2, we find,

$$\begin{aligned} dW_s = dF_s &= -\mathbf{M} \cdot d\mathbf{B} \\ &= HdB \text{ assuming } \mathbf{H} \text{ is always parallel to } \mathbf{B}. \end{aligned}$$

Above, $dF_s = dW_s$ represents the change in free energy density of the superconducting sample—doing work on the superconductor changes its free energy. Furthermore, in vacuum, $B = \mu_0 H$, so $dB = \mu_0 dH$. Thus,

$$dF_s = \mu_0 H dH.$$

Then, if we integrate both sides over appropriate bounds, we find,

$$\begin{aligned} \int_{F_s(0)}^{F_s(H^*)} dF_s &= \int_0^{H^*} \mu_0 H dH \\ = F_s(H^*) - F_s(0) &= \frac{\mu_0}{2} H^{*2} \end{aligned} \tag{2.3}$$

Another condition we must impose is that at the critical applied field strength H_c, $F_s(H_c) = F_n(H_c)$, where F_s is the superconducting free energy density and F_n is the "normal" free energy density. The equality of the free energy densities follows from the definition of thermodynamic equilibrium. So, by Equation 2.3,

$$F_n(H_c) = F_s(H_c) = F_s(0) + \frac{\mu_0}{2}{H_c}^2. \tag{2.4}$$

For a normal material, we have $F_n(H^*) = F_n(0)$ almost exactly (except for its intrinsic *demagnetization*, which we take to be negligible in this case). So, we can write the difference in free energy between the normal and superconducting states at absolute zero:

$$\begin{aligned}\Delta F_{sn} &= F_s(0) - F_n(0) \\ &= \left[F_s(H_c) - \frac{\mu_0}{2}{H_c}^2\right] - F_n(0) \\ &= \left[F_s(H_c) - \frac{\mu_0}{2}{H_c}^2\right] - F_n(H_c)\end{aligned}$$

Then, by Equation 2.4, we find:

$$\boxed{\Delta F_{sn} = -\frac{\mu_0}{2}H_c^2 = -\frac{1}{2\mu_0}B_{ac}^2.} \tag{2.5}$$

That is, the difference in free energy density between the normal and superconducting states—something akin to a binding energy—is proportional to the square of the critical magnetic field of a superconductor. B_{ac} is simply the applied magnetic field in units of Tesla, for ease of calculation. Let's give this equation some context: $B_{ac} = 0.0105$ Tesla at absolute zero for Aluminum [12]. This equates to a difference in free energy between the superconducting and normal states of 43 $\mathrm{J/m^3}$ at absolute zero. For an order of magnitude comparison, the energy density of one mole of material at room temperature from *thermal energy alone* is very roughly $F_n \sim N_A k_B T / \left(1\ \mathrm{m}^3\right) = (6.022 \times 10^{23})(1.38 \times 10^{-23})(300) \sim 2500\ \mathrm{J/m^3}$. Thus, thermal perturbations can easily destroy the superconducting state. However, at *low* temperatures ($T \sim 4.2$ K, the boiling point of helium,) the superconducting state is thermodynamically stable.

Now is a good time to remember the discussion in Chapter 1 on superconducting wavefunction symmetry. The wavefunction symmetry is sometimes referred to as the *energy gap symmetry* because the symmetries of the superconducting wavefunction determine the symmetries of the energy gap ΔF_{sn}. The above description of the superconducting energy gap

assumes implicitly that the energy gap is uniform across all superconducting states: ΔF_{sn} is independent of a given state's momentum, which can be described by the state's wave vector $\mathbf{k}$ in $\psi(\mathbf{r}) \sim \exp(i\mathbf{k}\cdot\mathbf{r})$ for plane wave states—this is like an s-wave superconductor. If, however, $\Delta F_{sn}(\mathbf{k})$ is a function of the wave vector $\mathbf{k}$, then the energy gap will be inherently *anisotropic*, as is the case in BaCo122 with its $s_{\pm}$-wave wavefunction symmetry, for example. The energy gap symmetry of a superconductor is a fundamental quantity of interest, and the above discussion gives a heuristic picture of the superconducting energy gap.

2.2 TYPES OF SUPERCONDUCTORS AND INTRINSIC LENGTH SCALES

The superconducting state of matter is thermodynamically stable, and we have quantified how H_c is an important quantity in the thermodynamic analysis of superconductors. Armed with the previous qualitative description of Type I and Type II superconductors, the task now is to quantify *what* differentiates these superconductors. For this, we will need to delve deeper into the quantum mechanics inherent to superconductivity. Specifically, we will define the coherence length and the London penetration depth. The first of these is easier to derive in a heuristic manner, so let's start our discussion with the coherence length.

2.2.1 *Coherence Length*

The superconducting state can be exactly described quantum mechanically using Ginzburg-Landau theory, but these theoretical tools are beyond the scope of this work. This being said, in order to precisely describe the differences between Type I and Type II superconductors, we must do *some* work with quantum mechanics. As a starting point, we assert that *all* of the superconducting charge carriers (Cooper pairs) can be nicely described by a single wavefunction.

In crystals, the basis functions for electronic wavefunctions are often taken to be plane waves (electrons are only loosely bound to the lattice, so this is an acceptable approximation.) We can write one of these wavefunctions as follows:

$$\varphi_0(x) = \exp(ikx),$$

where $k = 2\pi/\lambda$ is the wave vector. Now, consider the modulated wavefunction,

$$\varphi(x) = \frac{1}{\sqrt{2}}\left[\exp(i(k+q)x) + \exp(ikx)\right].$$

The parameter q quantifies the modulation to the wavefunction. Importantly, a modulation to the wavefunction represents a nonzero expectation value of kinetic energy for each superconducting electron. If this expectation value of kinetic energy exceeds the superconducting gap energy, superconductivity will no longer be thermodynamically favorable, and will be destroyed. We can write out the expectation value of the kinetic energy operator explicitly:

$$\begin{aligned}\left\langle \frac{p_x^2}{2m} \right\rangle &= \int_{\mathbb{R}} dx\ \varphi^* \left(-\frac{\hbar^2}{2m}\frac{d^2}{dx^2} \right) \varphi \\ &= \frac{1}{2}\left(\frac{\hbar^2}{2m}\right)\left[(k+q)^2 + k^2\right] \\ &\approx \frac{\hbar^2}{2m}k^2 + \frac{\hbar^2}{2m}kq\end{aligned}$$

We assume that the perturbation $q \ll k$ and only keep terms to first-order in q. The formal derivation of coherence length comes from Ginzburg-Landau theory, in which the superconducting wavefunction is investigated using something akin to first-order perturbation theory, so dropping higher-order terms in q is justified here. In any event, we can identify the modulation in the "normal" kinetic energy from this equation as the second term in the sum. At absolute zero, this modulation cannot be more than the energy gap E_g between the normal and superconducting state, lest superconductivity be destroyed. That is,

$$\frac{\hbar^2}{2m}k_F q_0 = E_g \tag{2.6}$$

Where k_F is the Fermi wave vector corresponding to the highest energy electrons at absolute zero. Now, we define the *intrinsic coherence length* $\xi_0 = 1/q_0$,

$$\xi_0 = \frac{\hbar^2 k_F}{2mE_g} = \frac{\hbar v_F}{2E_g} \tag{2.7}$$

The BCS theory of superconductivity yields the following very similar expression for the intrinsic coherence length:

$$\boxed{\xi_0 = \frac{2\hbar v_F}{\pi E_g}} \tag{2.8}$$

Notice: this coherence length is intrinsic to the material and its energy gap at absolute zero, which we calculated earlier to be proportional to the square of the critical field. **To be clear: the coherence length is the length scale over which the superconducting wavefunction can quickly vary before superconductivity is destroyed.**

2.2.2 *London Penetration Depth*

The second length scale we seek to quantify is the London penetration depth λ, which describes how deeply a magnetic field penetrates into a superconductor. The idea is this: due to boundary conditions imposed by Maxwell's equations, there cannot be a discontinuous change in magnetic induction $\mathbf{B}$, even at the interface of a superconductor and a normal material—$\mathbf{B}$ has to drop off continuously, and this decay has an associated length scale, λ.

In order to derive the London penetration depth, we need to define something known as *electromagnetic momentum*. Before even that, remember that the magnetic induction has a vector potential $\mathbf{A}$:

$$\mathbf{B} = \nabla \times \mathbf{A}.$$

Gauge invariance allows us to choose the divergence of $\mathbf{A}$. In this case, it is most useful to set $\nabla \cdot \mathbf{A} = 0$: this is known as the Coulomb gauge. There exist other gauges that are more useful for electrodynamics problems, but we needn't worry about these here. Applying Faraday's law, we see,

$$\nabla \times \mathbf{E} = -\frac{\partial}{\partial t}\mathbf{B} = -\frac{\partial}{\partial t}\left[\nabla \times \mathbf{A}\right].$$

From our choice of guage before, we have exactly,

$$\mathbf{E} = -\frac{\partial}{\partial t}\mathbf{A}.$$

In the presence of changing electric and magnetic fields, mechanical momentum $\mathbf{p} = m\mathbf{v}$ is not explicitly conserved in time. In order to fix this issue, we define the *electromagnetic momentum* in terms of the mechanical momentum and the magnetic vector potential:

$$\mathbf{p}_{EM} = m\mathbf{v} + q\mathbf{A}.$$

Then, we find,

$$\begin{aligned}\frac{d}{dt}\mathbf{p}_{EM} &= m\mathbf{a} + q\frac{\partial \mathbf{A}}{\partial t} \\ &= q\mathbf{E} - q\mathbf{E} = 0 \text{ by the Lorentz force law.}\end{aligned}$$

So, electromagnetic momentum is conserved in time. We now turn our focus to the superconducting current density, $\mathbf{j}_s$. Maxwell's equations require a shielding current on the surface of the superconductor that exactly cancels the applied magnetic field inside the material. So, we look to derive an expression for the magnetic field at the superconductor interface via the supercurrent density. As superconductivity is inherently a quantum-mechanical phenomenon, we need to make the following substitution:

$$j \to j_c \iff n_s q_s \mathbf{v}_s \to \frac{n_s q_s}{m_s} \left(\mathbf{p}_{EM} - q\mathbf{A}\right).$$

We define j_c as the quantum mechanical current operator, with $\mathbf{p}_{EM} = -i\hbar\nabla$ taking the place of the standard momentum operator. The density of superconducting states can be described by a wavefunction, so we have additionally $n_s \to \psi^*\psi$. Our supercurrent becomes,

$$\begin{aligned}\mathbf{j}_s &= \psi^* \frac{q_s}{m_s} \left[\mathbf{p}_{EM} - q_s\mathbf{A}\right] \psi \\ &= -\frac{q_s}{m_s} \left[i\hbar\psi^*\nabla\psi + \mathbf{A}\psi^*\psi\right].\end{aligned}$$

Here, note:

$$\begin{aligned}\nabla\psi &= \nabla|\psi| \exp(i\varphi) \\ &= i|\psi| \exp(i\varphi)\nabla\varphi + \exp(i\varphi)\nabla|\psi|\end{aligned}$$

Here, we make an approximation similar to that of WKB theory: we assert $\nabla|\psi| \ll \nabla\varphi$, i.e. the phase of the wavefunction φ varies quickly compared to the magnitude $|\psi|$, so we can neglect this second term. Thus,

$$\nabla\psi \approx i\psi\nabla\varphi.$$

Substituting this back into the earlier expression for the supercurrent density, we find,

$$\mathbf{j}_s = \frac{q_s n_s}{m_s} \left[\hbar\nabla\varphi - q\mathbf{A}\right].$$

The next step is to take the curl on both sides:

$$\begin{aligned}\nabla \times \mathbf{j}_s &= \frac{q_s n_s}{m_s} \left[\hbar\nabla \times (\nabla\varphi) - q_s\nabla \times \mathbf{A}\right] \\ &= \frac{q_s n_s}{m_s} \left[0 - q_s\nabla \times \mathbf{A}\right] \\ \Rightarrow \nabla \times \mathbf{j}_s + \frac{q_s^2 n_s}{m_s}\mathbf{B} &= 0. \qquad (2.9)\end{aligned}$$

Equation 2.9 is known as the London equation. This equation results from the assuming that the superconductor is a perfect conductor and can be described by one single wavefunction. We can use Equation 2.9 to derive an important result. For slowly-varying electromagnetic fields, Ampere's law without the Maxwell correction is valid (the quasi-static approximation). We first take the curl of both sides of the electrostatic/quasi-static form of Ampere's law:

$$\begin{aligned}\nabla \times (\nabla \times \mathbf{B}) &= \mu_0 \nabla \times \mathbf{j} \\ &= \mu_0 \nabla \times \mathbf{j} = \nabla (\nabla \cdot \mathbf{B}) - \nabla^2 \mathbf{B} \\ &= \nabla \times \mathbf{j} = -\frac{1}{\mu_0} \nabla^2 \mathbf{B}.\end{aligned}$$

Let's substitute this expression back into the London equation:

$$\nabla^2 \mathbf{B} = \frac{q_s^2 n_s \mu_0}{m_s} \mathbf{B} \tag{2.10}$$

We recognize this as an equation whose solution is an exponential. As noted, the magnetic field of a superconducting sample must drop off at some characteristic length scale. In light of Equation 2.10, we define the London penetration depth as follows:

$$\boxed{\lambda = \sqrt{\frac{m_s}{q_s^2 n_s \mu_0}}} \tag{2.11}$$

Such that,

$$\mathbf{B}(r) = \mathbf{B}_0 \exp(-\lambda / r)$$

at the superconductor interface. Importantly, λ depends on the mass, charge, and density of superconducting carriers.

2.3 WRAPPING UP

This chapter has been a brief overview of the concepts of superconductivity relevant to the material investigated in this work, BaCo122. There are a few main points to take away:

1. Superconductivity is thermodynamically stable. There exists an energy gap between the superconducting and normal energy states.
2. The coherence length ξ is the length scale over which the superconducting wavefunction can vary quickly.

3. The London penetration depth λ is the depth to which a magnetic field penetrates a superconductor.

4. Type I and Type II superconductors can be defined in terms of ξ and λ: for Type I, $\xi \gg \lambda$. For Type II, $\xi \ll \lambda$.

There is a lot of complex, intricate, and most importantly *interesting* math that goes into the quantum mechanics of superconductivity. Understanding novel superconductors, like BaCo122, will lead to a better understanding of superconductivity and physics as a whole.[1]

1 Thanks to Professor Heyman for notes on the London penetration depth, and Kittel for the explanation of the superconducting energy gap and coherence length [12].

3

NV CENTER THEORY

Now that we have discussed some fundamental superconductivity theory, we can move on to discussing the theory relevant to the experimental technique employed in this work, known as Nitrogen Vacancy center optical magnetometry, or NV center magnetometry for short. NV center magnetometry uses optical lasers and microwave radiation to gather information about magnetic fields. Lasers excite the NV center electronic state, and when this state relaxes, it emits red photons. The intensity of red fluorescence yields information on the applied magnetic field.

First, let's discuss what a nitrogen vacancy center *is*. A Nitrogen Vacancy (NV) center is a defect in diamond, as is shown in Figure 3.2. For the purposes of our experiment, we use NV centers that consist of six electrons in total; this system as a whole acts as a spin-1 quantum system. Because we can model NV centers as spin-1 quantum systems, we can precisely analyze how they work. In essence, the fluorescence of an excited NV center state depends on its spin quantum number m_s. Excited states with $m_s = 0$ always relax via emitting a red photon. Sometimes, excited states with $m_s = \pm 1$ relax *without* emitting a red photon. Furthermore, the magnetic dipole transition $m_s = 0 \rightarrow m_s = \pm 1$ corresponds to a photon of energy 2.87 GHz in zero applied magnetic field, as illustrated in Figure 3.3. If we excite the NV centers with green laser light, and then radiate them with microwave radiation of 2.87 GHz, we induce spin resonance between the $m_s = 0$ and $m_s = \pm 1$ states. This resonance causes a reduction in the fluoresced red photons, as illustrated in Figure 3.1.

If we now turn on a magnetic field, the degeneracy in the energy state of $m_s = \pm 1$ is lifted, and there are now *two* resonant microwave frequencies that cause the transitions $m_s = 0 \rightarrow -1$ and $m_s = 0 \rightarrow +1$. This is the reason there are two peaks in Figure 3.1 rather than just one. This degeneracy lifting is also illustrated in the pop-out in Figure 3.3.

The idea of the NV center technique is the following: we can induce spin resonance between the $m_s = 0$ and $m_s = \pm 1$ spin states in the ground state of the NV center, excite the NV centers with green laser light, and record red fluorescence as a function of microwave frequency. The difference in frequency between the fluorescence reduction peaks we see is proportional to the applied magnetic field, indicated as Z in Figure 3.1. In the context of a Type II superconductor, the frequency splitting Z gives us information its lower critical field H_{c1}.

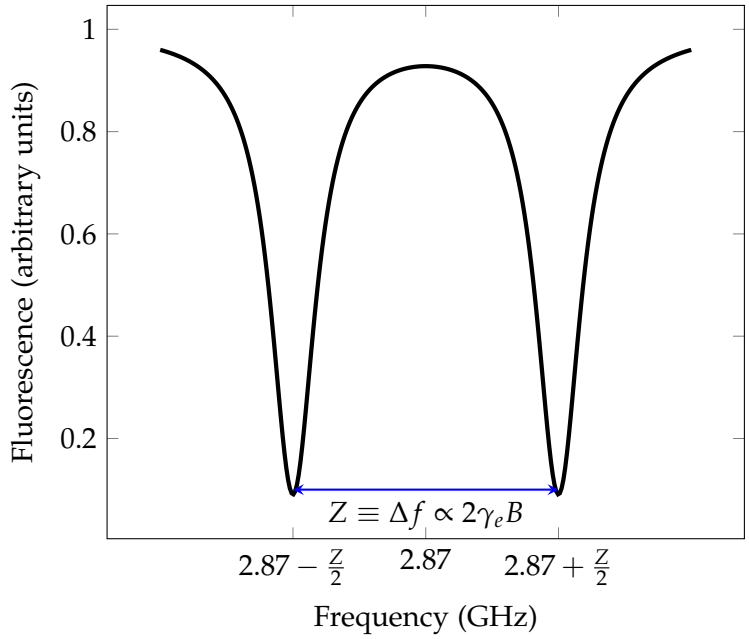

Figure 3.1: Idealized depiction of ODMR (optically detected magnetic resonance) in an NV center. Z is what's known as the "splitting" due to the magnetic field: the difference in energy between the two peaks. This Δf, when converted to an energy, is directly proportional to the magnetic field projected along the NV center unit vector. Here, we detect two peaks at two spin-resonant frequencies corresponding to the $m_s = 0 \rightarrow -1$ and $m_s = 0 \rightarrow +1$ states. The plot is centered around the zero-field splitting frequency $D \approx 2.87$ GHz.

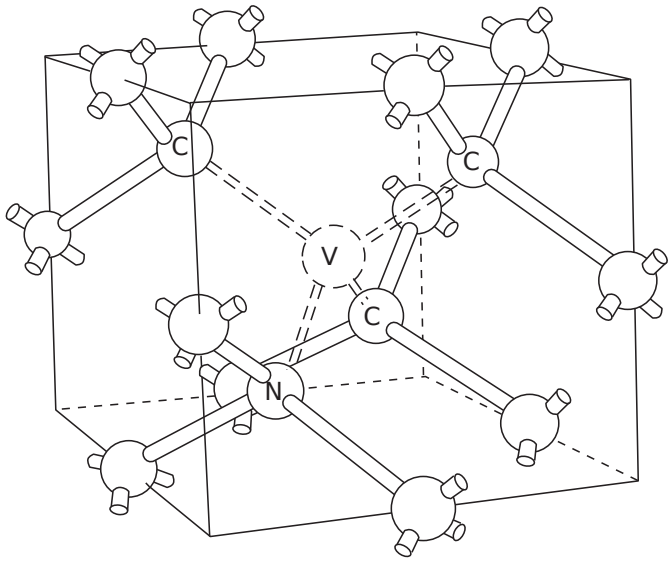

Figure 3.2: An NV center in the diamond lattice, oriented along a bond within the crystal lattice. A nitrogen atom is implanted in the diamond lattice, and a vacancy is formed adjacent to it. Then, the lattice is annealed, and the resulting NV void in the lattice becomes a system of six electrons with total spin 1. Image from Pushkarchuk et al. [19].

In the following sections, I will first describe the fundamental physics relevant to this treatment of NV centers. Next, I will explain how they can be used to very precisely measure magnetic fields via an optical technique. Finally, I will outline how they are used to investigate the magnetic properties of superconductors, which will be further developed in Chapter 5.

3.1 PHYSICS OF THE NITROGEN VACANCY CENTER

A Nitrogen Vacancy (NV) center is formed when a nitrogen atom replaces a carbon atom in the diamond crystalline lattice; in more precise terms, it is a point-like defect in the diamond lattice. The C$\rightarrow$ N replacement causes the lattice to distort, as can be seen in Figure 3.2, resulting in a void within the lattice. There are actually two types of NV center: NV[0] and NV[$-$], where the [0] and [$-$] correspond to the vacancy's net charge. Only NV[$-$] centers (which contain six electrons) can be used to measure magnetic fields, so henceforth when I refer to NV centers, I will implicitly be referring to NV[$-$] centers.

The energy levels of an NV center can be qualitatively understood via group theory. This group-theoretical treatment of energy is beyond the scope of this work, but the energy levels of the NV center are not: Figure 3.3 illustrates the energy levels of the NV center, as well as its

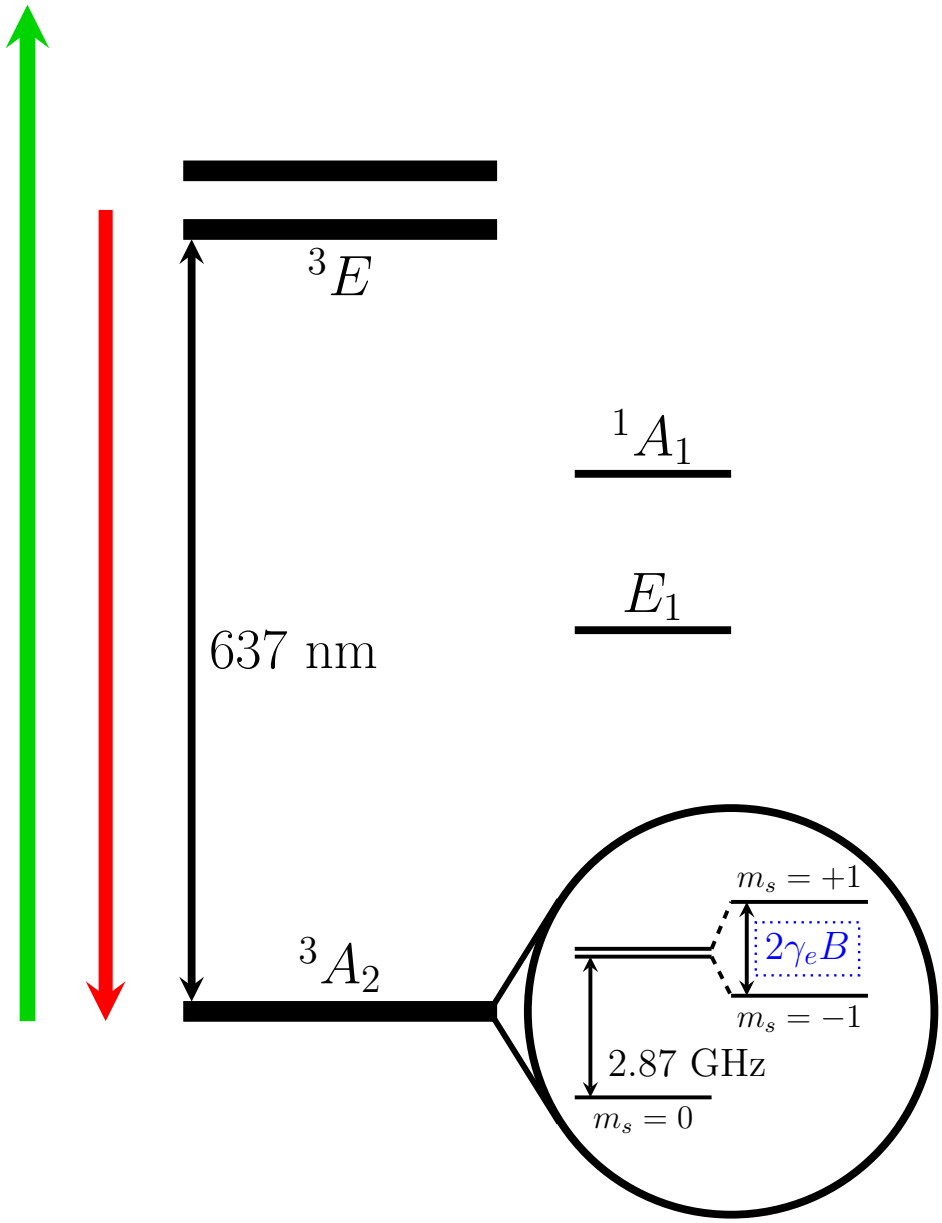

Figure 3.3: Energy level diagram for an NV center. We excite the NV ground state with green laser light, and the majority of electronic states (~ 70 %) relax from $^3E \rightarrow {}^3A_2$ by emitting 637 nm (red) photons. However, for electronic states with $m_s = \pm 1$, non-spin-conserving transitions may occur, in which a phonon carries away extra angular momentum, and the electronic state relaxes via $^3E \rightarrow {}^1A_1 \rightarrow E_1 \rightarrow {}^3A_2$, emitting *infrared* photons. The $m_s = \pm 1$ state splits in energy level proportional to the applied magnetic field, as indicated in the circular region. We drive resonance between the $m_s = 0$ and $m_s = \pm 1$ states with microwaves.

associated spin degeneracy lifting due to the Zeeman effect. The labels on the energy levels come from group theoretical considerations, but the diagram can be understood even without these labels.

This energy diagram can be better interpreted if we also look to the effective Hamiltonian of the NV center, given in Equation 3.1.

$$H_{\text{eff}} = DS_z^2 + E\left(S_x^2 - S_y^2\right) - \gamma_e \mathbf{S}\cdot\mathbf{B} \tag{3.1}$$

In this equation, the NV center is assumed to be oriented along the $\hat{\mathbf{z}}$ direciton. Thus, the term $D \approx 2.87$ GHz corresponds to an intrinsic on-axis (in the $\hat{\mathbf{z}}$ direction) energy, the term $E \approx 5$ MHz corresponds to *off*-axis energy due to crystalline strain, and $-\gamma_e \mathbf{S}\cdot\mathbf{B}$ corresponds to the perturbation to the Hamiltonian in the presence of a magnetic field. S_i represent the spin components (Pauli matricies) [15].

Equation 3.1 details the NV center Hamiltonian assuming that the NV center is oriented along the $\hat{\mathbf{z}}$ direction. However, inside diamond, this is not the most helpful description. The NV center orientation is determined by a vector connecting the lattice vacancy to the Nitrogen atom in the crystalline lattice. We can write out the four possible orientations of the NV center, directly computed from the diamond lattice vectors [15]:

$$\hat{\mathbf{d}}_1 = \frac{1}{\sqrt{3}}(-1,-1,-1) \qquad \hat{\mathbf{d}}_2 = \frac{1}{\sqrt{3}}(1,1,-1)$$
$$\hat{\mathbf{d}}_3 = \frac{1}{\sqrt{3}}(1,-1,1) \qquad \hat{\mathbf{d}}_4 = \frac{1}{\sqrt{3}}(-1,1,1)$$

These vectors are of *particular* importance because of how we ultimately use NV centers to measure magnetic fields: the optical feedback we receive from the NV centers comtains information about the *projection* of the magnetic field along the NV center axis, $\mathbf{B}\cdot\mathbf{d_i}$. In order to discuss the relevance of these vectors in more detail, we must discuss how we use NV centers to measure magnetic fields, and the various optical elements involved.

3.2 NV CENTER OPTICAL MAGNETOMETRY

In Figure 3.3, there are a few arrows: red, green, and black arrows corresponding to light of different wavelengths in the optical and microwave regimes. This is because when we use NV centers to measure magnetic fields, we are using them as *optical magnetometers*—that is, we use light to measure the magnetic properties of a given sample. The process can be outlined as follows:

1. Apply a fixed magnetic field $\mathbf{H}$ perpendicular to the *ab* plane, as indicated in Figure 3.5. Then,

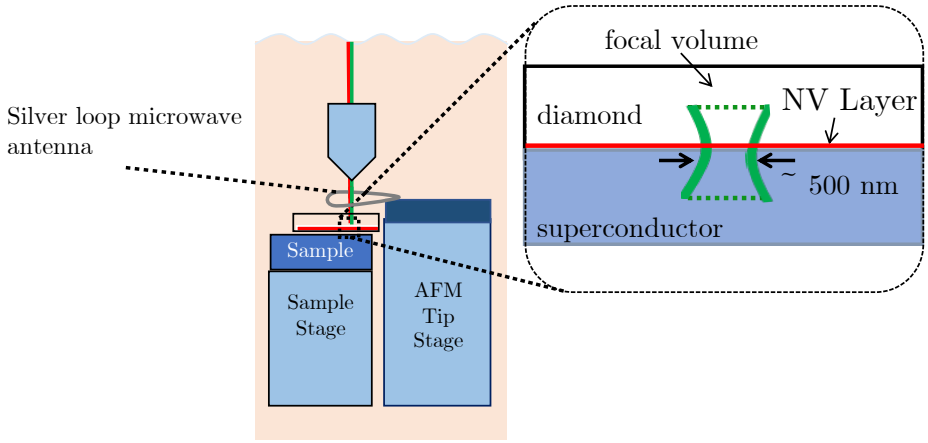

Figure 3.4: Schematic of the experimental setup when the sample is in position. The wire loop radiates microwaves which cause spin resonance via magnetic dipole transitions in the NV centers. The diamond-sample interface is in the focal volume of the confocal microscope. Optical feedback is collected from this focus.

a) Radiate the diamond containing many NV centers (which is situated on top of a superconducting sample, as in Figure 3.4) with continuous-wave microwaves of fixed frequency near $f \sim 2.87$ GHz. 2.87 GHz corresponds to frequencies near the on-axis zero-field energy parameter D from the NV Hamiltonian, given in Equation 3.1.

b) Excite the NV centers with green laser light of known power.

c) Measure *only* the red photons emitted by the NV centers as the electronic states relax (we use a light filter to remove other colors).

d) Record the relative power received. Power received will be lower, as in Figure 3.1, when there is resonance between the $m_s = 0$ and $m_s = \pm 1$ states.

e) Increment the microwave frequency and repeat.

2. Increment the magnetic field and repeat.

We repeat this process until we are confident that the magnetic field is penetrating the superconducting sample.

The simplest response possible from an NV center would be for a magnetic field $\mathbf{B} = B_0 \hat{\mathbf{d}}_\mathbf{i}$, i.e. the magnetic field we're interested in lies completely along an NV direction. In this case, the recorded intensity of red photons would look something like Figure 3.1. In practice, the magnetic field does not maintain its orientation completely along the direction of the NV centers: the NV centers are randomly oriented in the diamond

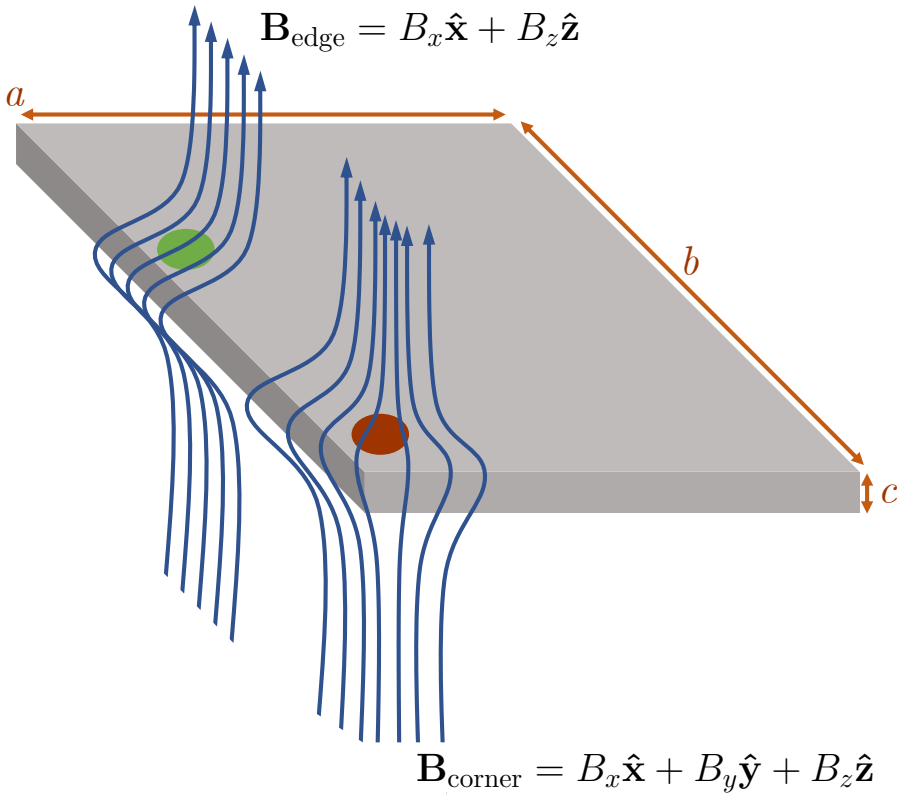

Figure 3.5: We measure the superconducting sample at a region like the green spot. In this region, **B** has only two components, so we only observe two pairs of Zeeman splitting due to the projection of **B** along the NV axes. At the corner, the magnetic induction has three components, so measuring here would make it more difficult to interpret our result.

along all four possible $\mathbf{d_i}$, and the magnetic field has multiple spatial components, as shown in Figure 3.5. So, we end up with information on the projection of the magnetic field along the NV center axis, $\mathbf{B} \cdot \mathbf{d_i}$. We only gain information about the *projection* of the field because only the field components along the direction of the NV center spin lead to the Zeeman effect energy splitting: the Zeeman effect Hamiltonian goes like $H_Z \sim -\gamma_e \mathbf{B} \cdot \mathbf{S}$.

Because we gain information on the projection of **B** along an NV center orientation, we choose to measure the magnetic field at the center of an edge, as shown in Figure 3.5, as opposed to a corner. When we measure at an edge, we only need to worry about the B_z and B_x components of the field. If we assume $\mathbf{B} = B_x\hat{\mathbf{x}} + B_z\hat{\mathbf{z}}$, then we can write the projections along the NV directions as follows:

$$\mathbf{B}\cdot\mathbf{d_1} \propto -(B_x + B_z) \qquad \mathbf{B}\cdot\mathbf{d_2} \propto B_x - B_z$$
$$\mathbf{B}\cdot\mathbf{d_3} \propto B_x + B_z \qquad \mathbf{B}\cdot\mathbf{d_4} \propto -(B_x - B_z)\,.$$

The energy *difference* between the $m_s = \pm 1$ states induced by Zeeman splitting as shown in Figure 3.3 only depends on the *magnitude* of the applied magnetic field. So, in actuality, we end up with only two relevant "energy splittings",

$$Z_s = |B_x + B_z| \qquad Z_d = |B_x - B_z| \tag{3.2}$$

where Z_s corresponds to the *sum* Zeeman energy splitting, and Z_d corresponds to the *difference* Zeeman energy splitting. Z_s and Z_d are commonly referred to as *splittings* for shorthand, because they represent splittings in energy of the $m_s = \pm 1$ states.

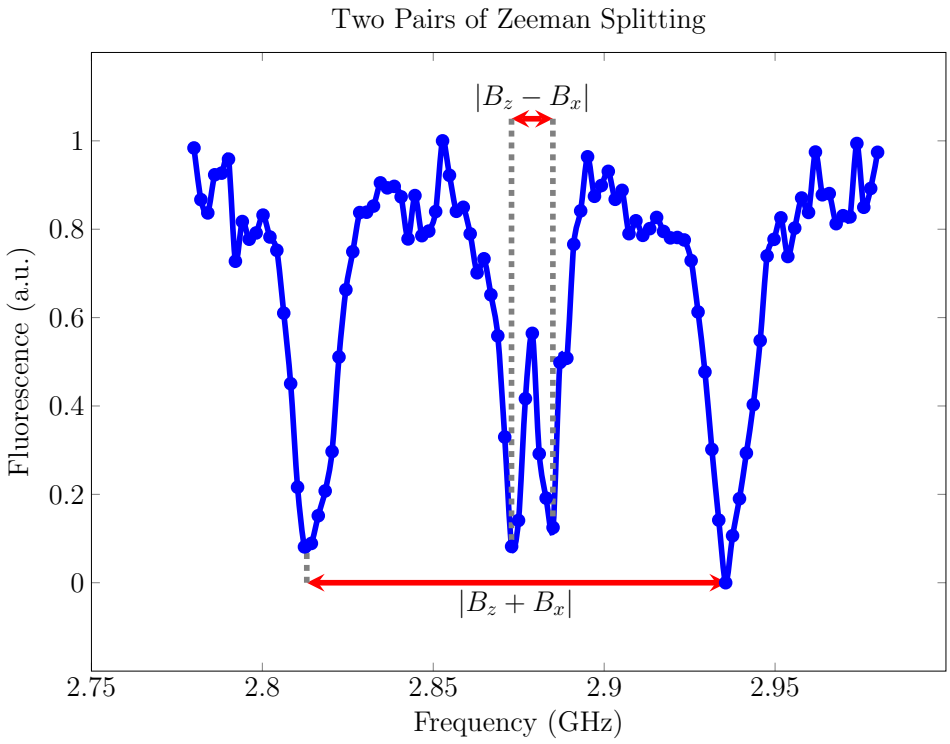

Figure 3.6: We detect two pairs of splitting when $\mathbf{B} = B_x\hat{\mathbf{x}} + B_z\hat{\mathbf{z}}$.

The core of NV magnetometry relies on the splitting of the $m_s = \pm 1$ state. Illustrated in Figure 3.1 is the detected splitting for **B** oriented along an NV axis. A more realistic example can be seen in Figure 3.6. This example, using NV center data collected from Pb (courtesy of Naufer Nusran and Kamal Joshi, Ames Lab), illustrates the reduced fluorescence at the two pairs of spin-resonant frequencies, labeled Z_d and Z_s.

The quantity relevant to measuring the lower critical field is Z_d. We monitor Z_d because it remains constant when there is no magnetic penetration and increases linearly when there is penetration (i.e. when there is a larger $\hat{\mathbf{z}}$ component). Z_s increases linearly in both cases, which is not as helpful. We can monitor Z_d through various applied field strengths to detect when magnetic field begins to leak in at the edge of a superconductor; this leakage indicates that the superconducting state is becoming less stable. In fact, the field at which we detect non-baseline splitting we call H_p, and from this we can calculate the lower critical field H_{c1}. This analysis technique is further developed in Chapter 6.

In all, NV centers provide a minimally-invasive way to measure the magnetic properties of superconductors with diffraction-limited precision. NV$[-]$ centers can be treated as spin-1 systems and obey the Zeeman effect. We can exploit the optical fluorescence of NV centers in conjunction with the Zeeman effect and optically-detected magnetic spin resonance (ODMR) to extract information about the projection of magnetic fields along the NV orientation axis. **In short: we can use lasers and NV centers to learn about magnetic fields near superconductors in a noninvasive way.**

Part II

EXPERIMENT

4

HYPOTHESES

In this chapter, we will discuss two hypotheses relating to measuring the properties of BaCo122 using NV center magnetometry. These hypotheses are mainly concerned with the capabilities of NV centers.

4.1 TEMPERATURE-DEPENDENT NV CENTER MAGNETOMETRY

Before this work, NV center magnetometry had only been employed at Ames National Laboratory to measure the London penetration depth λ of superconductors at a base temperature of 4.2 K. Varying or raising this temperature could have adverse affects on the NV center measurement:

- The microwave antenna could distort, impacting NV center spin resonance.
- The sample could thermally expand underneath the diamond slab containing NV centers and distort Zeeman splitting detection.

Thus, using NV center magnetometry to measure the London penetration depth λ at various temperatures is a nontrivial task. We hypothesize that NV center magnetometry can be used to measure the London penetration depth λ at temperatures above the base temperature of 4.2 K (the boiling point of liquid He). **This work marks the first time that NV center magnetometry has been used to measure λ as a function of temperature, to the best of our knowledge.**

4.2 NV CENTER MAGNETOMETRY VS. BULK TECHNIQUES

Crystals are imperfect, especially near the edges: lattices terminate inelegantly, and there can be distortion between crystal layers even if the sample has been cleaved nicely. One advantage of the NV center technique is that we can use it to pick and locally probe a "good" portion of a crystal. We screen several candidate samples using a scanning electron microscope, paying particular attention to sample edges, and choose one with reasonably well-defined shape for NV measurements.

The local nature of the NV center technique distinguishes it from others that measure the entire sample in bulk, such as the tunnel diode resonator (TDR) technique. To be clear, the TDR technique measures the *entire* sample, all at once. In one sense, this gives a better overall picture of the defining

properties of the sample, such as its critical temperature T_c, its London penetration depth λ, and its lower and upper critical fields H_{c1} and H_{c2}. However, the defects that plague the whole crystal will plague a bulk measurement.

We hypothesize that NV center magnetometry will yield results distinct from bulk measurements due to inherent differences between local and bulk techniques.

5

PROCEDURE

We use NV center magnetometry in conjunction with confocal microscopy to measure the lower critical field H_{c1} and absolute value of the penetration depth λ in the superconductor $Ba\left(Fe_{1-x}Co_x\right)_2 As_2$, $x = 7.4\%$ (BaCo122). The current iteration of this technique consists of a few key stages. We obtain our sample from Dr. Canfield's crystal synthesis group at Ames Lab. We then carefully place the sample into an attoAFM/CFM cryogenic system. Using NV center magnetometry, we measure the superconducting transition of the sample, and then (indirectly) measure the lower critical field H_{c1} at four different temperatures; this last stage makes up the bulk of the experiment time.

5.1 SAMPLE PREPARATION AND EQUIPMENT ALIGNMENT

Before we perform any low-temperature measurements, we must take care to properly prepare the sample. A preliminary step is cleaving the sample to sizes that fit well in the experiment apparatus (area ~ 1 mm). We then use a scanning electron microscope to verify the sharpness of edges, as can be seen in Figure 5.1. Having sharp edges is important because we require the sample to have a well-defined geometry (more on this later).

We mount the BaCo122 sample onto a diamond substrate containing many NV centers, and then onto a piezoelectric sample stage. The stage can move the sample in all three spatial dimensions and has a resolution of about 0.1 nm. Figure 3.4 shows a schematic of the sample, diamond slab, and sample stage. We can vary the precision and speed of the sample stage positioning by varying the magnitude, duration, and frequency (pulses/second) of voltage pulses to the piezoelectric component of the sample stage.

We then carefully transfer this piezoelectric stage apparatus to the bottom of a mounting tube, below the focal volume of the confocal microscope used to collect red NV center fluorescence. Figure 5.2 shows the mounting tube, before and after sample placement. After positioning the photoactive NV region in the focal volume of the confocal microscope at room temperature, the combined tube is placed in an attoAFM/CFM cryogenic system for measurements.

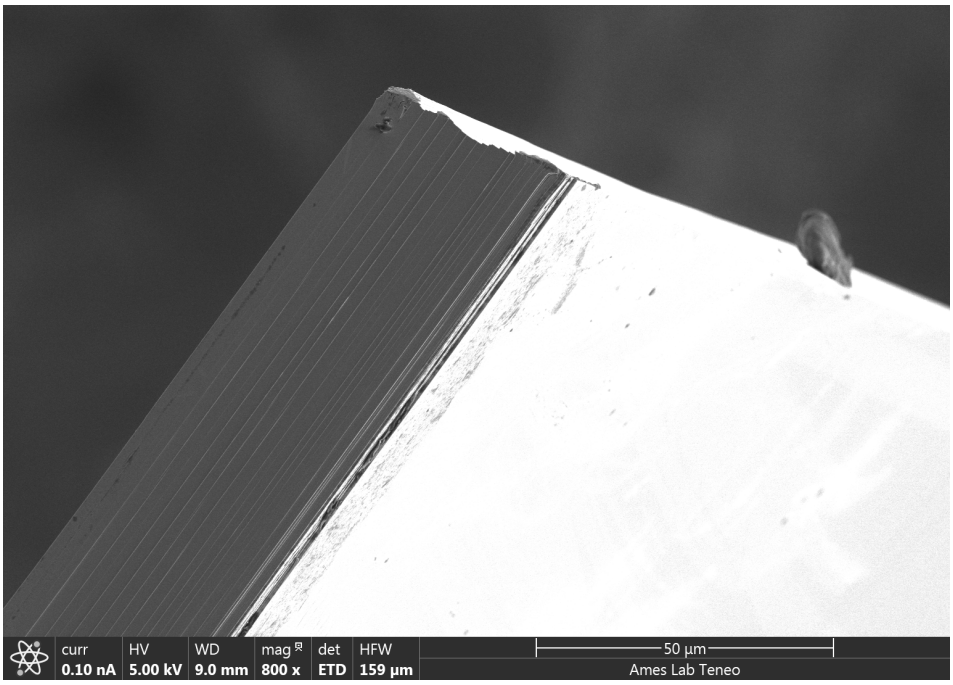

Figure 5.1: Sharp sample edges are important because of geometric considerations. Here, we verify the sharpness of the studied BaCo122 sample.

5.2 CRITICAL TEMPERATURE

As a first measurement, we verify the critical temperature of the BaCo122 sample to make sure our apparatus is configured correctly before moving on to the lower critical field H_{c1} measurements. In the case of this BaCo122 sample, our equipment was in good alignment, and we calculate a critical temperature of 22.2 ± 1 K, which is consistent with the literature [10].

To detect the superconducting transition, we first move the sample stage such that the confocal microscope volume is at the center of the sample.

Once we have positioned the confocal volume at the center of the superconducting sample, we heat the sample up to a temperature of 30 K using a thermoelectric heater with no applied magnetic field, and then cool it to the base temperature of 4.2 K to ensure that all Abrikosov vortices have dissipated. Heating through and above the transition temperature destroys superconductivity, allowing supercurrents and trapped vortices to dissipate. Cooling in zero-field conditions allows the sample to enter a superconducting state with no vortices present.

After cooling the sample, a constant applied field $\mathbf{H} = 10\hat{\mathbf{z}}$ Oersted (Oe) is applied perpendicular to the sample surface. (Side note: Oe is the cgs unit of $\mathbf{H}$ and Gauss (G) is the cgs unit of $\mathbf{B}$). We then record the Zeeman splitting at the base temperature. To do this, we shine green laser light

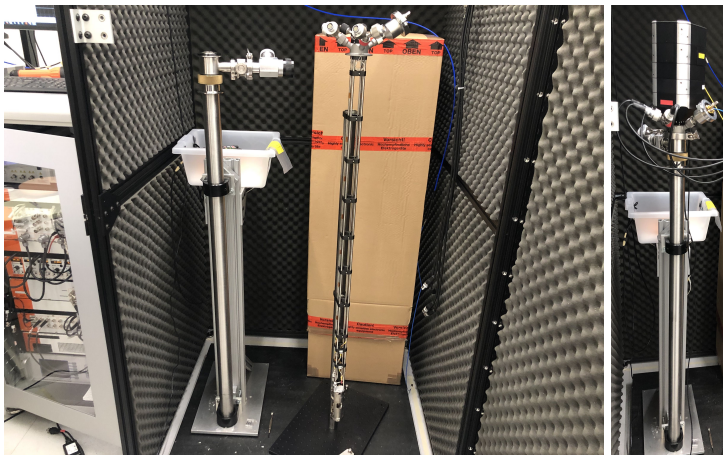

Figure 5.2: Left: sample mounting tube (right) and vacuum tube (left). Right: mounting tube inside vacuum tube.

onto the NV centers; this provides us with the red optical fluorescence that we record as our signal. After recording a signal from the NV centers at the base temperature, we heat the sample, wait for the temperature to stabilize, and repeat the process. We continue this procedure until we observe a dramatic increase in either Z_s or Z_d, which corresponds to the superconducting transition. The superconducting transition we measured can be seen in Figure 5.4.

As a note: in this case, we don't really care which pair of Zeeman splitting we detect; we can observe either Z_s or Z_d. As shown in Figure 5.3, the magnetic field around the center of the sample is nearly zero. Thus, $Z_s \propto |B_x + B_z|$ and $Z_d \propto |B_x - B_z|$ are both nearly zero before the superconducting transition ($B_x \sim B_z \sim 0$), and both positive afterwards (the magnetic field penetrates the sample).

5.3 LOWER CRITICAL FIELD

After we align our equipment and verify the integrity of our sample via the diagnostic critical temperature measurement, we perform the lower critical field H_{c1} measurements—the bulk of our experimental procedure. We perform these measurements at 5 K, 10 K, 15 K, and 17 K, and observe how the lower critical field changes with temperature. The closer we are to the critical temperature T_c, the less stable the superconducting state is, so we should expect H_{c1} to decrease with temperature.

We set the sample temperature using a thermoelectric heater, and then orient the confocal volume at the edge of the superconducting sample. As diagrammed by Figure 3.5, if we collect feedback from the NV centers at the center of the sample near an edge, we only need worry about the $\hat{\mathbf{x}}$

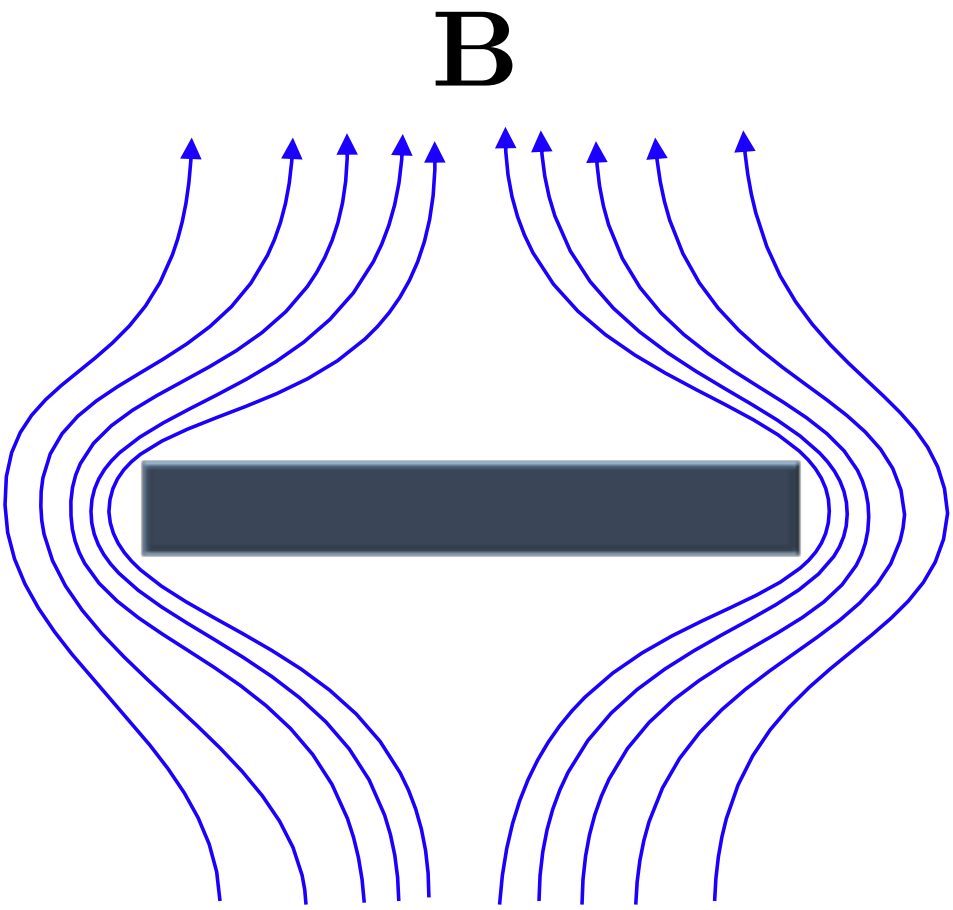

Figure 5.3: Magnetic fields are expelled by a superconducting sample. Because of this flux expulsion, the field is nearly zero at the center of the sample.

and $\hat{\mathbf{z}}$ components of the field, which simplifies the interpretation of our measurements. Further, measuring a few hundred microns from the edge of the sample allows us to detect with point-like accuracy the applied field strength at which magnetic fields begin to leak into the sample. If we can determine this applied field strength at which the magnetic field begins to leak into the edges of the sample, we can calculate the lower critical field H_{c1} and the penetration depth λ.

Once the sample temperature has stabilized and our equipment has been oriented at a position like the green spot in Figure 3.5, we begin our magnetic field measurement. We shine green laser light onto the NV center/superconductor interface; again, this laser light "pumps" the NV centers, causing them to fluoresce, and this microwave-dependent fluorescence is the optical feedback we detect. We apply a constant, weak magnetic field $\mathbf{H} = H_z\hat{\mathbf{z}}$, $|\mathbf{H}| \sim 5$ Oe, perpendicular to the sample surface.

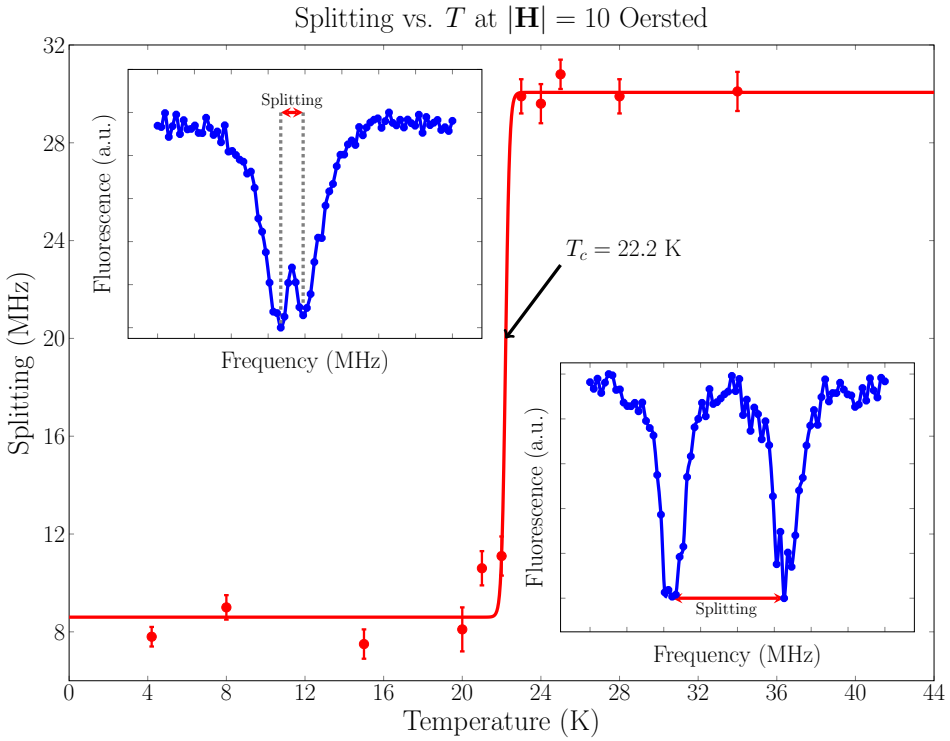

Figure 5.4: Superconducting transition as detected by NV magnetometry. Below the critical temperature, the signal we receive looks like the left inset. Above the critical temperature, our signal looks like the right inset. As we move through the superconducting transition, more magnetic field begins to penetrate the sample, so our Zeeman splitting response widens.

Then, we radiate microwaves of fixed frequency, measure the response from the NV centers, and increment this frequency. The range of frequencies we use is approximately 2.8 to 2.95 GHz, and we use a frequency step size of about 10 MHz. We record the optical feedback from the NV centers using a photon counter within the confocal microscope enclosure (pictured at the top of Figure 5.2).

Each measurement (at fixed T and H) averages over about 200 runs, and we repeat the measurement at four points along the edge, spaced a few microns apart. We then average the measurements corresponding to these four *physical* points to obtain a single *data* point, which roughly translates to the superconductor's ability to shield the applied magnetic field at a particular temperature, field strength (T, H) pair.

We repeat this process at fixed temperature with varying field strength until we begin to see a response from the NV centers that indicates an increased $\hat{\mathbf{z}}$ component of the magnetic field penetrating the sample. We observe this increase in $\hat{\mathbf{z}}$ component as a widening of fluorescence reduction peaks $Z_d \propto |B_z - B_x|$, like those in Figure 3.6. We call the field strength at which the applied magnetic field begins to *penetrate* the sample edges H_p. From this field strength, we can calculate the lower critical field H_{c1}, as well as the absolute value of the penetration depth λ.

In sum, the experimental procedure for measuring/calculating the lower critical field of a given superconducting sample using NV magnetometry consists of three main steps. First, we obtain a superconducting sample, mount it onto a piezoelectric sample stage, and position it at room temperature. We then cool the sample to liquid helium temperatures and measure its critical temperature T_c. We then measure the field strength at which magnetic fields begin to significantly leak into the edges of the superconducting sample H_p, from which we calculate the lower critical field H_{c1} and the penetration depth λ of the superconductor at hand, in our case $\mathrm{Ba}\left(\mathrm{Fe}_{1-x}\mathrm{Co}_x\right)_2\mathrm{As}_2$, $x = 7.4\%$.

6 RESULTS

We first verify the quality of our BaCo122 sample by measuring its superconducting transition. We find $T_c \approx 22.2 \pm 1$ K, in agreement with the literature [10]. Further, we are able to use NV magnetometry to measure the field at which Abrikosov vortices begin to leak into the edges of a superconducting sample, H_p, as a function of temperature. We find H_p decreases as $T \to T_c$, in agreement with intuition: a weaker field is required to make the superconducting state thermodynamically unfavorable the closer we are to the critical temperature. From these values of H_p, we calculate H_{c1} and λ for this sample of BaCo122. Our measured values of the absolute value of the penetration depth λ are consistent with other local probe techniques such as magnetic force microscopy (MFM) and muon spin resonance (μSR), but disagree at high T with bulk measurement techniques.

6.1 DETERMINING THE PENETRATIVE FIELD

The process of collecting the individual data points of H_p at a given (T, H) requires multiple steps of post-processing. As a first step, we need to extract the actual splitting between reductions in fluorescence, as for example those seen in Figure 3.6 indicated by $Z_d \propto |B_z - B_x|$. In order to reproducibly and effectively measure the frequency splitting of a sample, we fit a double Lorentzian function to the data, and extract a precise splitting $Z_d = \Delta f$ between the peaks, as well as the splitting error.

As a reminder, for each (T, H) pair, we measure four separate physical points at the edge of the sample and then take an average. Thus, we perform the double Lorentzian fit on the splitting data of each of these points, and average the resulting errors and splittings (which in turn have been averaged over about 200 measurements).

We recorded the splitting response at $T = 5$ K, 10 K, 15 K, and 17 K. The averaged data corresponding to these temperatures can be seen in Figure 6.1, Figure 6.2, Figure 6.3, and Figure 6.4. From these plots, we gauge the penetrating field H_p by eye: H_p corresponds to where the frequency splitting begins to differ from the baseline zero-field splitting level. There is some splitting with zero magnetic field applied due to crystalline strain (hence the nonzero average zero-field splitting).

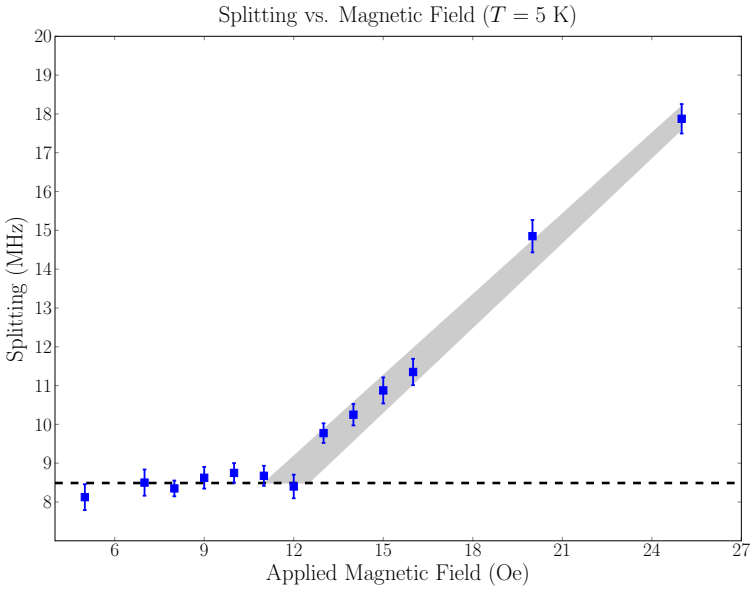

Figure 6.1: Determining H_p for $T = 5$ K. Black dashed lines indicate zero-field splitting (average). Gray areas roughly show the data spread.

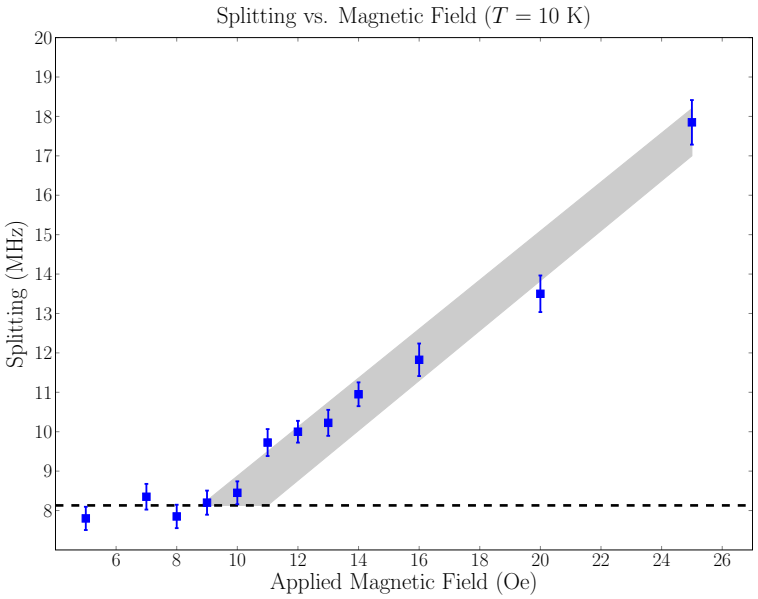

Figure 6.2: Determining H_p for $T = 10$ K. Black dashed lines indicate zero-field splitting (average). Gray areas roughly show the data spread.

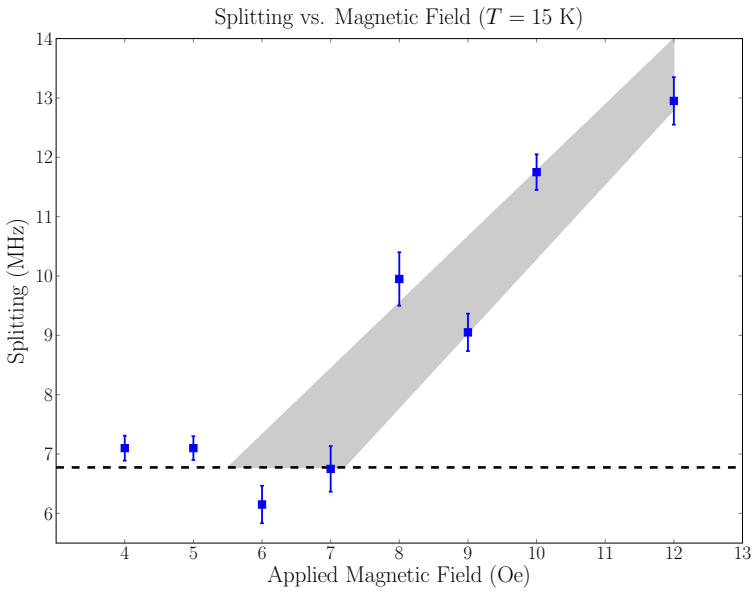

Figure 6.3: Determining H_p for $T = 15$ K. Black dashed lines indicate zero-field splitting (average). Gray areas roughly show the data spread.

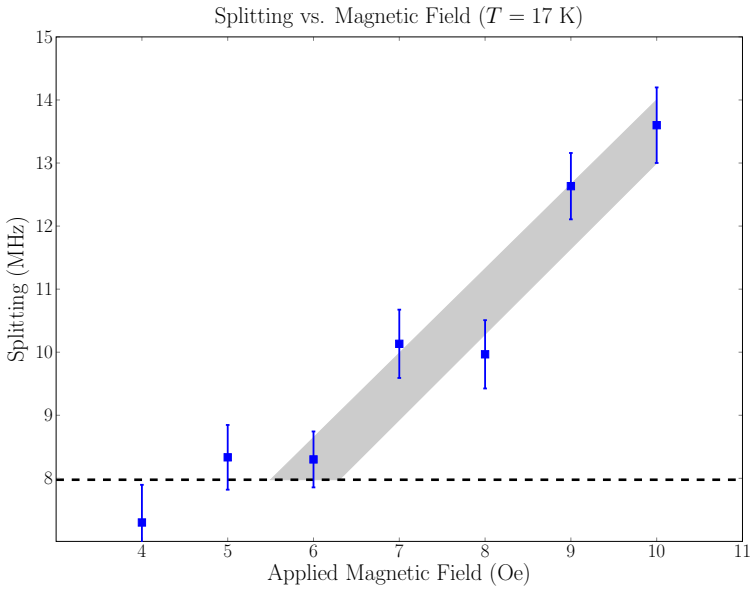

Figure 6.4: Determining H_p for $T = 17$ K. Black dashed lines indicate zero-field splitting (average). Gray areas roughly show the data spread.

T (K)	5	10	15	17
H_p (Oe)	12 ± 1	10 ± 1	7 ± 1	6 ± 1

Table 6.1: Measured H_p for each temperature of our BaCo122 sample.

6.2 LOWER CRITICAL FIELD AND LONDON PENETRATION DEPTH FROM THE PENETRATIVE FIELD

The penetrative field H_p directly yields the lower critical field as well as the absolute value of the London penetration depth. We calculate these values using Equation 6.2 and Equation 6.3, given by Prozorov and Kogan, and Hu, respectively [8, 17]. Here, a, b, and c correspond to the sample dimensions like shown in Figure 3.5, and N is a geometric demagnetization factor. Φ_0 is the magnetic flux quantum, and ξ is the superconducting coherence length. These equations are solved numerically for the lower critical field H_{c1} and the London penetration depth λ. Values for ξ were calculated using Equation 6.1 with data from Gordon et al. and Ni et al. [5, 14].

$$H_{c2} = \frac{\Phi_0/2}{\pi\xi^2} \tag{6.1}$$

$$N = \left[1 + \frac{3c}{4a}\left(1 + \frac{a}{b}\right)\right]^{-1} \tag{6.2}$$

$$H_{c1} = \frac{H_p}{1-N} = \frac{\Phi_0}{4\pi\lambda^2}\left[\ln\left(\frac{\lambda}{\xi}\right) + 0.497\right] \tag{6.3}$$

From an optical microscope image, we find the horizontal sample dimensions are as follows: $a = 720 \pm 5$ nm; $b = 810 \pm 5$ nm. Using an electron microscope image and a plane fit in Mathematica, we find $c = 36 \pm 5$ nm.

We calculate the temperature-dependent lower critical fields and absolute values of the London penetration depth for this BaCo122, $x_{\mathrm{Co}} = 7.4\%$ as given in Table 6.2. As can be seen in Figure 6.5, the penetration depths are in good agreement with other probe-based techniques, but diverge somewhat from the bulk measurement TDR technique at $T >\sim 10$ K. For these comparisons, we only need to worry about the value of the penetration depth λ, as it encodes information equivalent to H_{c1}: ξ only depends on H_{c2}, by Equation 6.1.

Details of the error analysis for these plots can be found in Appendix A.

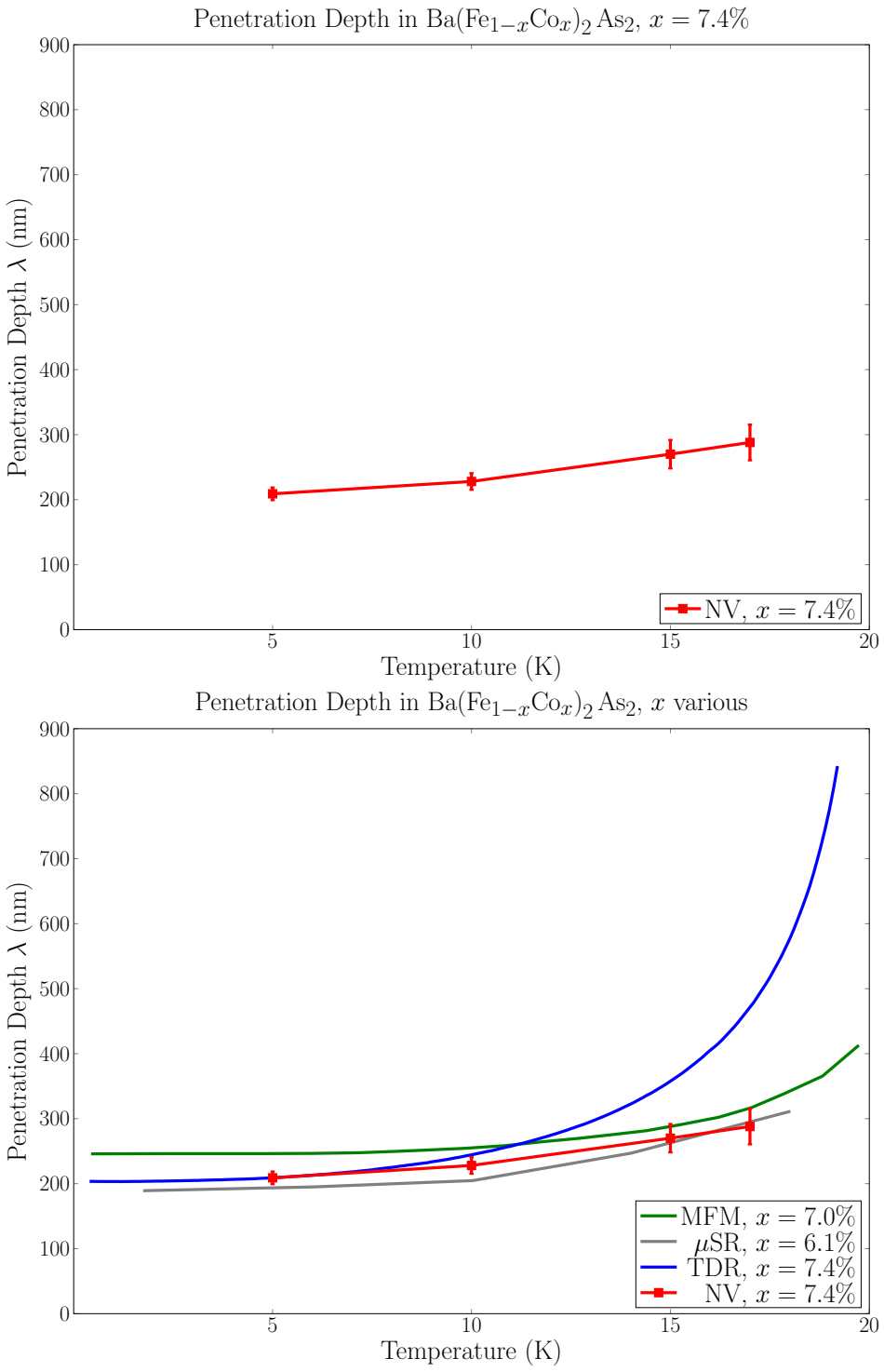

Figure 6.5: Top: $\lambda\,(T)$ as measured by NV magnetometry in this BaCo122 sample. Bottom: $\lambda\,(T)$ per NV as compared with other techniques.

T (K)	5	10	15	17
H_{c1} (Oe)	181 $\pm$15	151 $\pm$15	105 $\pm$15	90 $\pm$15
λ (nm)	209 $\pm$9.8	228 $\pm$12.8	270 $\pm$21.9	288 $\pm$27.5

Table 6.2: Values of lower critical field H_{c1} and London penetration depth λ for the BaCo122 sample as measured at four different temperatures below T_c by the NV magnetometry technique.

Part III

DISCUSSION AND CONCLUSIONS

7

ANALYSIS OF THE LOWER CRITICAL FIELD AND PENETRATION DEPTH

7.1 FITTING THE CRITICAL TEMPERATURE AND ZEEMAN SPLITTINGS

In order to estimate the critical temperature of the superconductor, we perform a sigmoid fit on our data. This fit takes the form given in Equation 7.1, where C_0, C_1, T_c, and δT_c are fitting parameters. We didn't take many data points for the critical temperature stage of this experiment: this stage was diagnostic. Because there are so few data points, we set $\delta T_c = 0.1$ so our fit doesn't yield erroneous results. In any event, we use Mathematica to fit our NV data to get an estimate of T_c, which we find to be $T_c \approx 22.2 \pm 1$ K. The uncertainty on this measurement is taken to be the standard error given by the Mathematica fit. If we had been more careful and taken many more data points, we could have reduced the error on T_c. In effect: the error on T_c is likely lower than 1 K, even though Mathematica reports this error to be so high. However, our primary science goal was to measure the lower critical field H_{c1}, not the critical temperature T_c, so this is ok.

$$S(t) = C_0 + \frac{C_1}{1 + \exp\left(-(T - T_c)/\delta T_c\right)} \tag{7.1}$$

The Zeeman splittings plotted in Figure 6.1, Figure 6.2, Figure 6.3, and Figure 6.4 were calculated from a double Lorentzian function fit. This function essentially has two upside down peaks of variable width and center. A schematic of a possible fit can be seen in Figure 3.1. We then take the splittings to be the difference in the minima of the two peaks, taking care to fit the Z_d splitting—this splitting gives us information on the magnetic induction's penetration into the sample. We gauge H_p and its error by eye, and propagate error as discussed in Appendix A.

7.2 DIFFERENCES BETWEEN LOCAL AND BULK TECHNIQUES

We find that the critical temperature measurements of our BaCo122 sample are in agreement with those found in the literature, namely $T_c \approx 22.2$ K [10]. We also find that the penetration depths as determined by NV center magnetometry are in good agreement with other local probe techniques such as muon spin relaxation and magnetic force microscopy, as can be

seen in Figure 6.5. We see discrepancies between the local measurement techniques and bulk TDR technique at $T >\sim 10$ K.

The interpretation of these discrepancies is qualitatively straightforward, but difficult to quantify exactly. NV center magnetometry offers a minimally-invasive technique for measuring the absolute (actual) vale of the London penetration depth of a given superconductor. MFM is like a magnetically-active AFM, and μSR involves firing muons at a target and recording how their spins evolve through the crystalline lattice. So, one would expect NV magnetometry to yield slightly different results from MFM and μSR measurements, which inherently perturb the system more strongly due to their magnetic interactions. At temperatures lower than $T \sim 15$ K, the techniques differ by tens of nanometers. At temperatures higher than about 15 K, the techniques agree within the margin of error. Overall, these local probe techniques—techniques that look at isolated parts of the sample, rather than the whole thing all at once—are in qualitative agreement at all temperatures measured.

At low T, we can see in Figure 6.5 that the NV result and the tunnel diode resonance (TDR) result align perfectly. This is an artefact of comparing these techniques: TDR only measures the *change* in London penetration depth relative to its value at absolute zero, unlike NV center magnetometry which yields the *absolute value* of λ. Aligning these measurement techniques should thus be valid: TDR in theory yields $\Delta\lambda = \lambda_{\mathrm{NV}} - \lambda(0)$, i.e. the TDR measurement should be offset from the NV measurement by a constant, $\lambda(0)$. This being said, the two techniques narrowly agree within the margin of error at $T = 10$ K, and diverge for $T >\sim 10$ K.

One explanation of this divergence is that TDR is inherently a *bulk technique*. The TDR technique yields extremely precise values for the change in penetration depth relative to its value at absolute zero $\Delta\lambda(T)$, but (importantly) it measures the properties of the entire sample all at once. Figure 5.1 shows the very clean, sharp edge of a superconductor that we used to measure H_p and thus calculate H_{c1} and λ. Thus, the "version" of the superconductor that we look at with the NV technique is more ideal than the one seen by the TDR technique.

7.3 NV CENTER MAGNETOMETRY VS. TDR AND SQUID (BULK) TECHNIQUES

NV centers can measure near-ideal portions of superconductors, but cannot factor in the effects of bulk disorder. In fact, much of the work of Ruslan Prozorov's group at Ames Laboratory has been focused on the effect of disorder introduced via electron irradiation in superconducting samples using the TDR technique. However, the disorder introduced by electron irradiation almost certainly affects the results of the TDR measurement

differently than other forms of bulk crystalline defects, such as lattice distortion at the edges—this kind of distortion allows for easier magnetic field penetration. In any event, there are fundamental differences between the sample that the NV centers "see" and the sample the TDR "sees": the version that the NV centers investigate contains fewer defects. The effects of crystalline lattice disorder on TDR measurements is a area of research at Ames Laboratory.

As another test of the idea of local vs. bulk technique, we measured the superconducting transition of our BaCo122 sample with a different bulk technique. We measured the transition using a device known as a Superconducting Quantum Interference Device (SQUID). We did not use this technique to measure the lower critical field of the sample, but we can still use this transition data to roughly compare the overall properties of the local probe and bulk measurement techniques. As can be seen in Figure 7.1, the NV center superconducting transition occurs at slightly higher T_c, where $T_c^{\mathrm{NV}} - T_c^{\mathrm{TDR}} \approx 1.1$ K and $T_c^{\mathrm{NV}} - T_c^{\mathrm{SQUID}} \approx 0.8$ K. The superconducting transition is measured to occur, in bulk, at around $T_c \approx 21.5$ K, but we calculate a critical temperature of around $T_c \approx 22.2$ K using NV center magnetometry. A one-Kelvin difference is outside the margin of error of the TDR and SQUID measurement techniques. This is further evidence of some kind of intrinsic difference between bulk measurement techniques and local probe techniques.

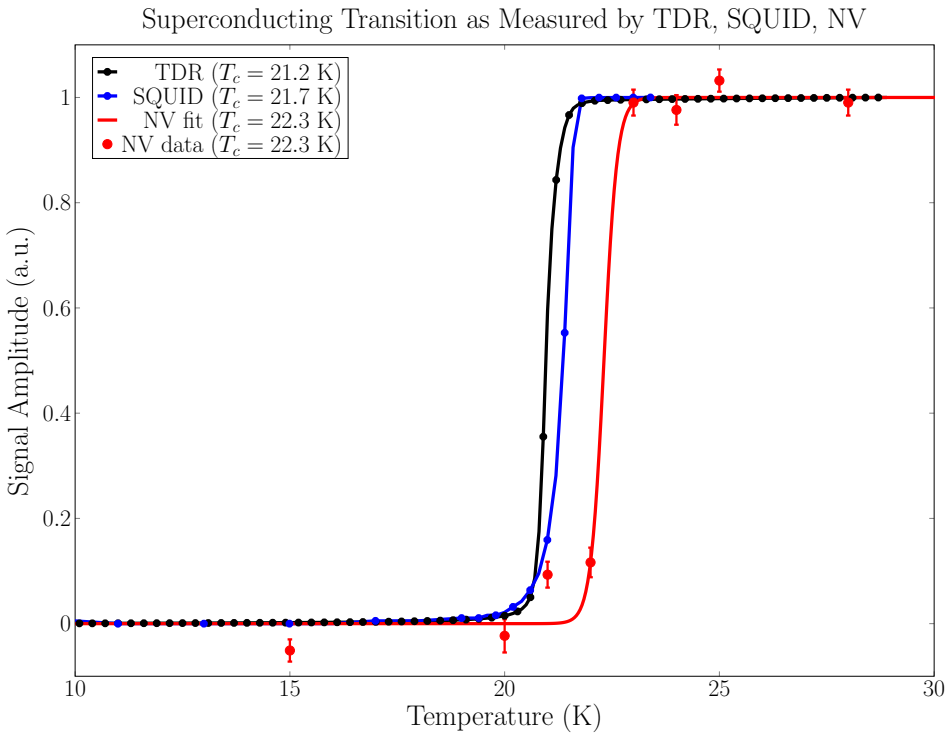

Figure 7.1: Comparing the superconducting transitions of TDR, SQUID, and NV techniques. Notably, the NV transition occurs at a slightly higher critical temperature than that of SQUID or TDR.

8

CONCLUSIONS

In this work, we have shown how NV center magnetometry can be used as an effective tool to investigate the properties of superconductors, and compared this technique with others. In all, our values of λ and H_{c1} are consistent with other probe-based techniques, like muon spin relaxation and magnetic force microscopy. There exists a discrepancy between the NV and TDR techniques at relatively high T, which may be due to crystalline defects. More work is required to concretely understand the discrepancy between the NV and bulk techniques.

We have shown that NV centers in diamond can be an effective tool for measuring the intrinsic properties of superconductors, such as the London penetration depth λ and the lower critical field H_{c1}. NV center magnetometry shows promise moving forward as another robust technique available to probe superconductors.

As evidenced in Figure 6.5, there is a discrepancy between the NV center magnetometry and TDR techniques which becomes especially apparent at high T. Further, in Figure 7.1, we see mutual agreement between the two bulk techniques (SQUID and TDR) relative to the NV technique. In short: there is a difference between probe-based and bulk techniques. An overarching reason for this difference can be summarized in one term: *crystalline imperfections*. Quantitative analysis of this problem is one of the ongoing research programs at the Ames Laboratory.

9 FUTURE WORK

NV center magnetometry has proven itself as an effective method for probing superconductor parameters. This being said, it has room for improvement. Additionally, more work must be done to determine the underlying physics of Fe-based pnictide superconductors, 112 iron arsenides in particular.

One avenue of development for NV centers would be to incorporate so-called *pulsed wave NV magnetometry*, in contrast to the continuous-wave technique employed in this work. This technique is more physically and mathematically complex, and involves encoding information into the phase of the NV center spin. This technique allows for greater signal-to-noise than the continuous wave technique [2].

Another idea for development would be to develop a single-NV center probe. This would allow for incredibly high spatial resolution, permitting direct imaging of Abrikosov vortices, which would yield direct information on the coherence length, for example. This can be achieved by essentially attaching a single NV center to an AFM tip and scanning the probe across a surface.

The scanning NV probe may also be able to reveal some information about the BaCo122 wavefunction symmetry. As mentioned in the introduction, the wave function of BaCo122 is widely believed to possess $s_{\pm}$ symmetry. This means that the angular part of the superconducting wavefunction changes sign for electron-like and hole-like superconducting charge carriers. There may be more structure encoded in the angular part, too; the argument of the angular part of the superconducting wavefunction (called the *phase*) may vary in a coherent way that is currently undetectable with common techniques. A scanning NV probe may be able to detect these phase fluctuations, which would be a very exciting discovery. The scanning NV technique is currently under investigation at Ames Lab.

Finally, more experiments are required to fully understand the complex physics underlying the superconductivity in 122 iron arsenides. These superconductors are complex: they undergo structural transitions under certain temperatures and pressures, and can transition from superconducting to antiferromagnetic ordering. The complexity of these superconductors is what makes them so interesting and novel. They are an embodiment of what 21st century physics will likely tackle: very hard, very complicated problems that can only be solved through the application of state-of-the-art knowledge and the innovative development of new physics.

Part IV

BACKMATTER

A

ERROR ANALYSIS FOR THE LOWER CRITICAL FIELD AND LONDON PENETRATION DEPTH

Errors for H_{c1} were calculated in the standard way. For errors in λ, upper and lower bounds on H_p were used to solve Equation 6.3 and errors were estimated from the difference in the bounded and reported value.

Errors on H_p are estimated by eye to be ± 1 Oe in each case. Errors on the sample dimensions, labeled in Figure 3.5, are estimated from the camera resolution. The expression for N is given by Equation 6.2. We use the standard error propagation estimate given by Equation A.1 to propagate the errors.

$$\sigma_x^2 \approx \left(\sigma_u \frac{\partial f}{\partial u}\right)^2 + \left(\sigma_v \frac{\partial f}{\partial v}\right)^2 + \cdots \tag{A.1}$$

Using this relation, we estimate the error in $1/N = 1.071$ to be $\sigma_{1/N} \approx 0.00698$, which translates to an error in N of $\sigma_N \approx 0.00609$. Using the relationship given by Equation 6.3, we can estimate the error of H_{c1} from the error in H_p and N. Table A.1 tabulates these errors. We can see that N contributes a fractional uncertainty of less than one percent, while H_p contributes a fractional uncertainty of about 10%. Thus, the error in H_{c1} and subsequently λ is dominated by the error in H_p—this will be important later.

The expression used to solve numerically for λ, given in Equation 6.3, is transcendental. Thus, standard error analysis techniques are not valid. Additionally, the expression given in Equation 6.3 relating H_{c1} to λ sensitively depends on the value of H_{c1}. Modifying H_{c1} by 15 Oe (which corresponds to the error in H_{c1}) causes Equation 6.3 to produce erroneous results for λ, giving $\lambda \sim 10^{-2}$ nm at $H_{c1} \pm \sigma_{Hc1}$—this is unphysical. So, we take a different approach to estimate the error in λ.

T (K)	H_p (Oe)	σ_{Hp} (Oe)	H_{c1} (Oe)	σ_{Hc1} (Oe)	σ_N/N	σ_{Hp}/H_p
5	12	1	181.41	15.16	0.65%	8.33%
10	10	1	151.18	15.15	0.65%	10.00%
15	7	1	105.82	15.13	0.65%	14.29%
17	6	1	90.71	15.13	0.65%	16.67%

Table A.1: Errors and fractional uncertainties relevant to the error in H_{c1}.

T (K)	H_p (Oe)	σ_{Hp} (Oe)	λ (nm)	λ_- (nm)	λ_+ (nm)	σ_λ (nm)
5	12	1	209.28	219.68	200.14	9.8
10	10	1	227.91	241.71	216.088	12.8
15	7	1	269.66	293.94	250.22	21.8
17	6	1	289.08	320.16	265.11	27.5

Table A.2: Errors and recalculated values relevant to the error in λ.

As can be seen in Table A.1, the majority of the uncertainty in H_{c1} comes from the uncertainty in H_p. Because H_{c1} encodes the same information as λ, and because most of our uncertainty comes from H_p, it is reasonable to estimate the error in λ using the uncertainty in H_p, rather than in H_{c1}. This approach produces reasonable results for λ, and a usable estimate of the uncertainty. In short: we calculate $\lambda(H_p)$, $\lambda(H_p + \sigma_{Hp})$, $\lambda(H_p - \sigma_{Hp})$. Then, we estimate σ_λ as follows:

$$\sigma_\lambda \approx \frac{\left|\lambda(H_p) - \lambda(H_p + \sigma_{Hp})\right| + \left|\lambda(H_p) - \lambda(H_p - \sigma_{Hp})\right|}{2}.$$

The errors are tabulated in Table A.2. The spreadsheet used to propagate these errors can be found here (hyperlink).

BIBLIOGRAPHY

[1] Marcus W Doherty, Neil B Manson, Paul Delaney, Fedor Jelezko, Jörg Wrachtrup, and Lloyd CL Hollenberg. "The nitrogen-vacancy colour centre in diamond." In: *Physics Reports* 528.1 (2013), pp. 1–45.

[2] A. Dréau, M. Lesik, L. Rondin, P. Spinicelli, O. Arcizet, J.-F. Roch, and V. Jacques. "Avoiding power broadening in optically detected magnetic resonance of single NV defects for enhanced dc magnetic field sensitivity." In: *Phys. Rev. B* 84 (19 2011), p. 195204. DOI: 10.1103/PhysRevB.84.195204. URL: https://link.aps.org/doi/10.1103/PhysRevB.84.195204.

[3] Adwaele English Wikipedia. *English: Flux lines in a type two superconductor01*. Wikipedia, 2012. URL: https://commons.wikimedia.org/wiki/File:Flux_lines_in_a_superconductor01.jpg.

[4] Atsushi Fujimori. *High-temperature superconductivity*. URL: http://wyvern.phys.s.u-tokyo.ac.jp/f/Research/hts_en.htm.

[5] RT Gordon, N Ni, C Martin, MA Tanatar, MD Vannette, H Kim, GD Samolyuk, J Schmalian, S Nandi, A Kreyssig, et al. "Unconventional London penetration depth in single-crystal Ba (Fe 0.93 Co 0.07) 2 As 2 superconductors." In: *Physical review letters* 102.12 (2009), p. 127004.

[6] PJ Hirschfeld, MM Korshunov, and II Mazin. "Gap symmetry and structure of Fe-based superconductors." In: *Reports on Progress in Physics* 74.12 (2011), p. 124508.

[7] Philip Hofmann. *Solid state physics: an introduction*. John Wiley & Sons, 2015.

[8] Chia-Ren Hu. "Numerical Constants for Isolated Vortices in Superconductors." In: *Phys. Rev. B* 6 (5 1972), pp. 1756–1760. DOI: 10.1103/PhysRevB.6.1756. URL: https://link.aps.org/doi/10.1103/PhysRevB.6.1756.

[9] K. R. Joshi, N. M. Nusran, M. A. Tanatar, K. Cho, S. L. Bud'ko, P. C. Canfield, R. M. Fernandes, A. Levchenko, and R. Prozorov. *Quantum phase transition inside the superconducting dome of $Ba(Fe_{1-x}Co_x)_2As_2$ probed by optical magneto-sensing using NV-centers in diamond*. 2019. arXiv: 1903.00053 [cond-mat.supr-con].

[10] K.R. Joshi, N.M. Nusran, M.A. Tanatar, Kyuil Cho, W.R. Meier, S.L. Bud'ko, P.C. Canfield, and R. Prozorov. "Measuring the Lower Critical Field of Superconductors Using Nitrogen-Vacancy Centers in Diamond Optical Magnetometry." In: *Phys. Rev. Applied* 11 (1 2019), p. 014035. DOI: 10.1103/PhysRevApplied.11.014035. URL: https://link.aps.org/doi/10.1103/PhysRevApplied.11.014035.

[11] H Kamerlingh Onnes. "The resistance of pure mercury at helium temperatures." In: *Commun. Phys. Lab. Univ. Leiden, b* 120 (1911).

[12] Charles Kittel. *Introduction to Solid State Physics*. 8th ed. Wiley, 2004. ISBN: 97804714152 68. URL: http://www.amazon.com/Introduction-Solid-Physics-Charles-Kittel/dp/047141526X/ref=dp_ob_title_bk.

[13] Lan Luan, Thomas M. Lippman, Clifford W. Hicks, Julie A. Bert, Ophir M. Auslaender, Jiun-Haw Chu, James G. Analytis, Ian R. Fisher, and Kathryn A. Moler. "Local Measurement of the Superfluid Density in the Pnictide Superconductor $Ba(Fe_{1-x}Co_x)_2As_2$ across the Superconducting Dome." In: *Phys. Rev. Lett.* 106 (6 2011), p. 067001. DOI: 10.1103/PhysRevLett.106.067001. URL: https://link.aps.org/doi/10.1103/PhysRevLett.106.067001.

[14] Ni Ni, ME Tillman, J-Q Yan, A Kracher, ST Hannahs, SL Bud'Ko, and PC Canfield. "Effects of Co substitution on thermodynamic and transport properties and anisotropic H c 2 in Ba (Fe 1- x Co x) 2 As 2 single crystals." In: *Physical Review B* 78.21 (2008), p. 214515.

[15] NM Nusran, Kamal R Joshi, Kyuil Cho, Makariy A Tanatar, William R Meier, SL Bud'ko, Paul C Canfield, Yong Liu, Thomas A Lograsso, and Ruslan Prozorov. "Spatially-resolved study of the Meissner effect in superconductors using NV-centers-in-diamond optical magnetometry." In: *New Journal of Physics* 20.4 (2018), p. 043010.

[16] Warren E Pickett. "Timing is crucial." In: *Nature Physics* 5.2 (2009), pp. 87–88.

[17] R. Prozorov and V. G. Kogan. "Effective Demagnetizing Factors of Diamagnetic Samples of Various Shapes." In: *Phys. Rev. Applied* 10 (1 2018), p. 014030. DOI: 10.1103/PhysRevApplied.10.014030. URL: https://link.aps.org/doi/10.1103/PhysRevApplied.10.014030.

[18] Ruslan Prozorov and Russell W Giannetta. "Magnetic penetration depth in unconventional superconductors." In: *Superconductor Science and Technology* 19.8 (2006), R41.

[19] V Pushkarchuk, Sergei Kilin, A.P. Nizovtsev, Alexander Pushkarchuk, V E. Borisenko, C von Borczyskowski, and AB Filonov. "Ab initio modeling of the electronic and spin properties of the [NV]- centers in diamond nanocrystals." In: *Optics and Spectroscopy* 99 (Aug. 2005), pp. 245–256. DOI: 10.1134/1.2034611.

[20] T. J. Williams et al. "Superfluid density and field-induced magnetism in $Ba(Fe_{1-x}Co_x)_2As_2$ and $Sr(Fe_{1-x}Co_x)_2As_2$ measured with muon spin relaxation." In: *Phys. Rev. B* 82 (9 2010), p. 094512. DOI: 10.1103/PhysRevB.82.094512. URL: https://link.aps.org/doi/10.1103/PhysRevB.82.094512.

COLOPHON

This document was typeset using the typographical look-and-feel `classicthesis` developed by André Miede and Ivo Pletikosić. The style was inspired by Robert Bringhurst's seminal book on typography "*The Elements of Typographic Style*". `classicthesis` is available for both LaTeX and LyX:

https://bitbucket.org/amiede/classicthesis/

Happy users of `classicthesis` usually send a real postcard to the author, a collection of postcards received so far is featured here:

http://postcards.miede.de/

Thank you very much for your feedback and contribution.

Final Version as of May 4, 2020 (classicthesis v4.6).